

# Mononuclear phagocytes locally specify and adapt their phenotype in a multiple sclerosis model

Giuseppe Locatelli<sup>1,2,10</sup>, Delphine Theodorou<sup>1,2,10</sup>, Arek Kendirli<sup>1,2</sup>, Marta Joana Costa Jordão<sup>3</sup>, Ori Staszewski<sup>3</sup>, Kshiti Phulphagar<sup>4</sup>, Ludovico Cantuti-Castelvetri<sup>5,6</sup>, Athanasios Dagalakis<sup>1</sup>, Alain Bessis<sup>7</sup>, Mikael Simons<sup>5,6,8</sup>, Felix Meissner<sup>4</sup>, Marco Prinz<sup>3,9</sup> and Martin Kerschensteiner<sup>1,2,8\*</sup>

**Mononuclear phagocytes are key regulators of both tissue damage and repair in neuroinflammatory conditions such as multiple sclerosis. To examine divergent phagocyte phenotypes in the inflamed CNS, we introduce an *in vivo* imaging approach that allows us to temporally and spatially resolve the evolution of phagocyte polarization in a murine model of multiple sclerosis. We show that the initial proinflammatory polarization of phagocytes is established after spinal cord entry and critically depends on the compartment they enter. Guided by signals from the CNS environment, individual phagocytes then switch their phenotype as lesions move from expansion to resolution. Our study thus provides a real-time analysis of the temporospatial determinants and regulatory principles of phagocyte specification in the inflamed CNS.**

Mononuclear phagocytes, including monocyte-derived macrophages and local microglia, play a crucial role in the pathogenesis of neuroinflammatory conditions like multiple sclerosis (MS)<sup>1,2</sup>. In this disease, they are the dominant cell type encountered in lesions<sup>3</sup>, their presence and activation correlates with the emergence of tissue damage<sup>4</sup>, and many of them are found in close apposition to damaged axons or in the process of phagocytosing myelin<sup>5</sup>. The contribution of mononuclear phagocytes to autoimmune CNS inflammation is further underlined by studies in disease models showing that their depletion prevents CNS lesion formation<sup>6</sup> and that interfering with monocyte influx or with microglia activation curtails disease progression<sup>7,8</sup>. In reverse, the central or peripheral activation of phagocytes alone is sufficient to induce the formation of inflammatory CNS lesions<sup>9,10</sup>. While phagocytes are thus a central force that drives the formation of inflammatory lesions, the same cells are probably an equally important contributor to lesion recovery, as they can dampen CNS inflammation and support both axonal regeneration and myelin repair<sup>11–13</sup>.

How can the same cell type have such seemingly opposing effects on the CNS environment? A concept that might help explain this apparent contradiction proposes that phagocytes can acquire distinct phenotypes that are characterized by divergent molecular arsenals, metabolic states, and effector functions<sup>14,15</sup>. In this concept, phagocytes with a proinflammatory polarization (often referred to as a classically activated or M1 phagocytes) release high levels of toxic mediators, including reactive species, and contribute to CNS damage<sup>16</sup>, while anti-inflammatory (often termed alternatively activated or M2) phagocytes are molecularly adapted for phagocytosis of tissue debris and the support of CNS repair<sup>13,17</sup>. This functional dichotomy is reflected on the molecular level by a pair of signature

enzymes that compete for the intracellular substrate L-arginine. Proinflammatory phagocytes express the signature enzyme iNOS (inducible nitric oxide synthase) and use arginine to generate the reactive species nitric oxide (as well as L-citrulline), while the anti-inflammatory signature enzyme arginase catalyzes the generation of urea, L-ornithine, and ultimately polyamines, substrates that contribute to tissue repair<sup>18</sup>. Whether and how this concept can explain phagocyte polarization and actions in neuroinflammatory lesions is still under debate<sup>19</sup>. In particular, we do not know how phagocyte phenotypes are specified in the CNS and whether such CNS phenotypes are stable or can change on the population level as well as on the single-cell level as the disease moves toward remission.

To address these questions, we established a phenotype imaging approach based on reporter mice that translate the pro- or anti-inflammatory polarization of phagocytes into distinct fluorescent signals. *In vivo* imaging in an animal model of MS then allowed us to follow the evolution of individual phagocyte phenotypes in different CNS compartments during the formation and resolution of inflammatory lesions. Our results show that both lesion stage and CNS compartment influenced the phagocyte polarization in neuroinflammatory lesions. Phagocytes acquired their initial polarization after CNS entry, and, as the disease evolved, individual phagocytes locally switched their phenotype by passing through a transitional state. A comprehensive molecular characterization of these distinct phenotypes revealed that CNS phagocytes differed in their mode of ATP generation, scavenging function, and capability to produce reactive species rather than in the expression of cytokines classically associated with pro- and anti-inflammatory phenotypes *in vitro*. The critical instructive role of the CNS environment was further emphasized by cell transfers showing that CNS-derived

<sup>1</sup>Institute of Clinical Neuroimmunology, University Hospital, Ludwig-Maximilians University Munich, Munich, Germany. <sup>2</sup>Biomedical Center, Ludwig-Maximilians University Munich, Munich, Germany. <sup>3</sup>Institute of Neuropathology, Freiburg University Medical Center, Freiburg, Germany. <sup>4</sup>Experimental Systems Immunology, Max Planck Institute of Biochemistry, Martinsried, Germany. <sup>5</sup>Institute of Neuronal Cell Biology, Technical University Munich, Munich, Germany. <sup>6</sup>German Center for Neurodegenerative Disease (DZNE), Munich, Germany. <sup>7</sup>Institute of Biology, Ecole Nationale Supérieure, Paris, France. <sup>8</sup>Munich Cluster for Systems Neurology (SyNergy), Munich, Germany. <sup>9</sup>BIOSS Centre for Biological Signalling Studies, University of Freiburg, Freiburg, Germany. <sup>10</sup>These authors contributed equally: Giuseppe Locatelli, Delphine Theodorou. \*e-mail: [martin.kerschensteiner@med.uni-muenchen.de](mailto:martin.kerschensteiner@med.uni-muenchen.de)

signals guided the local phenotype switch and by transwell experiments that identified astrocytes as a cellular source of such signals.

## Results

**Phenotypes of mononuclear phagocytes evolve over the course of experimental autoimmune encephalomyelitis.** To dynamically assess the evolution of phagocyte phenotypes in neuroinflammatory lesions, we made use of two complementary reporter mouse lines, in which the induction of signature enzymes that characterize pro- or anti-inflammatory phagocyte phenotypes result in distinct fluorescent labeling of the corresponding cells. We thus employed the iNOS-tdTomato-Cre mouse line<sup>20</sup>, which expresses a red fluorescent protein (tdTomato, as well as the Cre recombinase) under the control of the iNOS promoter, and the Arginase-YFP mouse line<sup>21</sup>, which expresses YFP under the control of the arginase promoter. We first cultured bone marrow-derived macrophages from these animals to confirm that a classical proinflammatory stimulation model (lipopolysaccharide (LPS) + interferon- $\gamma$  (IFN- $\gamma$ )) resulted in the expression of tdTomato but not of YFP, while alternative (anti-inflammatory) activation of cultured macrophages using a combination of interleukin (IL) 4 and IL13 led to selective expression of YFP. In contrast, cultured nonactivated phagocytes produced neither of the fluorescent proteins (Supplementary Fig. 1). In line with the latter finding, no reporter expression was observed in microglial cells in the healthy CNS, as analyzed by flow cytometry, immunofluorescence, or in vivo imaging (Supplementary Fig. 2).

In contrast, when double transgenic iNOS-tdTomato-Cre  $\times$  Arginase-YFP mice were induced with an animal model of MS, experimental autoimmune encephalomyelitis (EAE), fluorescently labeled cells appeared in the spinal cord. The vast majority of these cells were mononuclear phagocytes, as more than 90% of them were also positive for the phagocyte marker Iba-1, while no labeling of T cells, B cells, oligodendrocytes, astrocytes, or neurons was observed (Supplementary Fig. 3a–h). Immunohistochemical analysis further confirmed that the presence of the fluorescent label in these cells showed a close correlation to the expression of the corresponding signature enzymes (Supplementary Fig. 3i–l). Within spinal lesions we could thus differentiate M<sup>iNOS</sup> cells expressing tdTomato, M<sup>Arginase</sup> cells expressing YFP and M<sup>iNOS/Arginase</sup> cells expressing both markers. The vast majority of Iba1<sup>+</sup> cells showed such polarizations (see Methods). Quantitative analysis of neuroinflammatory lesions revealed that initially the accumulation of cells observed in the spinal cord and brain stem at earliest signs of EAE (weight loss) were dominated by M<sup>iNOS</sup> phagocytes (Fig. 1a,b and Supplementary Fig. 4). The proportions of these cells in the lesions then decreased progressively over the disease course, while M<sup>Arginase</sup> cells showed the reverse kinetics. Notably, in M<sup>iNOS/Arginase</sup> cells, the relative ratio of tdTomato versus YFP expression shifted over time, paralleling the shift of the entire phagocyte population and suggesting that these cells represent an intermediate polarization state.

In line with this view, the flow cytometric analysis of phagocytes isolated from the inflamed spinal cord revealed remarkable similarities between M<sup>iNOS</sup>, M<sup>iNOS/Arginase</sup>, and M<sup>Arginase</sup> cells in expression of lineage and activation markers, major histocompatibility complex (MHC) class II, co-stimulatory molecules, and cytokines such as TNF $\alpha$  and TGF $\beta$  (although IL1 $\beta$  expression and the IL1 $\beta$ /IL1ra ratio were primarily increased in M<sup>iNOS</sup> phagocytes; Fig. 1c–f). This expression pattern was distinct from the one observed in spinal cord microglia, and indeed, fate-tracking experiments in CCR2<sup>RFP/+</sup>  $\times$  CX3CR1<sup>GFP/+</sup> mice<sup>22</sup> revealed that more than 90% of polarized cells in neuroinflammatory lesions originated peripherally (Fig. 1g,h).

While M<sup>iNOS</sup>, M<sup>iNOS/Arginase</sup>, and M<sup>Arginase</sup> phagocytes share the same origin, specific differences in their molecular makeup exist. This view is supported by comprehensive transcriptional profiling of M<sup>iNOS</sup>, M<sup>iNOS/Arginase</sup>, and M<sup>Arginase</sup> cells sorted from early neuroinflammatory

lesions. While principal component analysis illustrated the close relation of these cell populations compared to nonpolarized phagocytes (Fig. 2a), the analysis of individual transcripts revealed a number of differentially regulated genes, including those encoding iNOS and arginase, as well as genes encoding a range of receptors, signaling molecules, and enzymes, many of which have not been previously associated with distinct phagocyte polarizations in vitro (Fig. 2b,c and Supplementary Fig. 5). Further analysis of candidate molecules highlighted that polarized CNS phagocytes differed in many molecular characteristics from resting microglia and blood monocytes, but were remarkably similar to one another with regards to the expression of activation marker and cytokines. Furthermore, while differentially polarized phagocytes isolated both from initial lesions (at the weight loss stage) and from lesions at the peak of disease appeared to shift their expression of genes encoding matrix metalloproteinases such as *Mmp12*, complement components such as *C1q*, and glycolytic enzymes, only a few of these changes reached statistical significance (Fig. 2d and Supplementary Fig. 6).

To further delineate the molecular pathways that differentiate pro- and anti-inflammatory phagocyte phenotypes in the CNS, we performed quantitative mass spectrometry analysis of M<sup>iNOS</sup>, M<sup>iNOS/Arginase</sup>, and M<sup>Arginase</sup> cells isolated from early neuroinflammatory lesions (Fig. 3). Subsequent bioinformatic comparison of the proteome of M<sup>iNOS</sup> and M<sup>Arginase</sup> cells provided further evidence indicating that differentially polarized phagocyte use alternative modes of ATP production. While M<sup>iNOS</sup> cells upregulated glycolysis and carbohydrate phosphorylation, M<sup>Arginase</sup> cells showed increased expression of multiple components of the mitochondrial electron transport chain required for oxidative phosphorylation (here annotated as ‘ubiquinone’). Furthermore, M<sup>iNOS</sup> cells showed increased expression of antimicrobial and antioxidant proteins, including the critical alarmins S100A8 and S100A9<sup>23</sup> and nearly all peroxiredoxins, a family of proteins that regulate release and detoxification of reactive species<sup>24</sup>. In contrast, M<sup>Arginase</sup> cells were characterized by upregulation of proteins (here annotated as ‘collagen’) that contribute to opsonization and scavenging of tissue debris, including the various C1q chains and the macrophage scavenger receptor 1 (CD204). Another family preferentially found in M<sup>Arginase</sup> cells was the EGF-like domain-containing protein family, which includes additional scavenging receptors such as stabilin 1, which has been shown to promote tissue homeostasis<sup>25</sup>, and proteins like thrombospondin, which can directly promote neuronal remodelling<sup>26</sup> and thereby nervous system recovery. Taken together, the comprehensive molecular characterization of differentially polarized CNS phagocytes indicated that they primarily differed in their metabolic states and in the way they interacted with the CNS environment, with M<sup>iNOS</sup> cells being equipped for the release of reactive species and M<sup>Arginase</sup> cells being primed for debris removal and tissue repair.

## Spatial regulation of phagocytes phenotypes in the spinal cord.

To better characterize how phagocyte phenotypes evolve in different CNS compartments, we imaged phagocytes in the upper meninges (dura and arachnoid mater), at the pia–parenchyma border, and in the spinal cord parenchyma at different timepoints over the course of EAE in living mice<sup>27</sup>. To locate phagocytes in these compartments, we first imaged a tissue volume starting at the meningeal surface before carefully removing the upper meninges with a forceps and re-acquiring the same volume (Fig. 4a and Supplementary Video 1). Phagocytes that were present at the first but not at the second imaging step were thus judged to be located in the upper meninges, while phagocytes at the pia–parenchyma border appeared on top of the spinal cord at the second imaging timepoint. Quantitative analysis of the in vivo recordings revealed a spatial gradient of phagocyte polarizations, with a significantly higher proportion of M<sup>iNOS</sup> cells and a lower proportion of M<sup>Arginase</sup> cells in the parenchyma compared to the upper meninges at peak of disease (Fig. 4b). In contrast

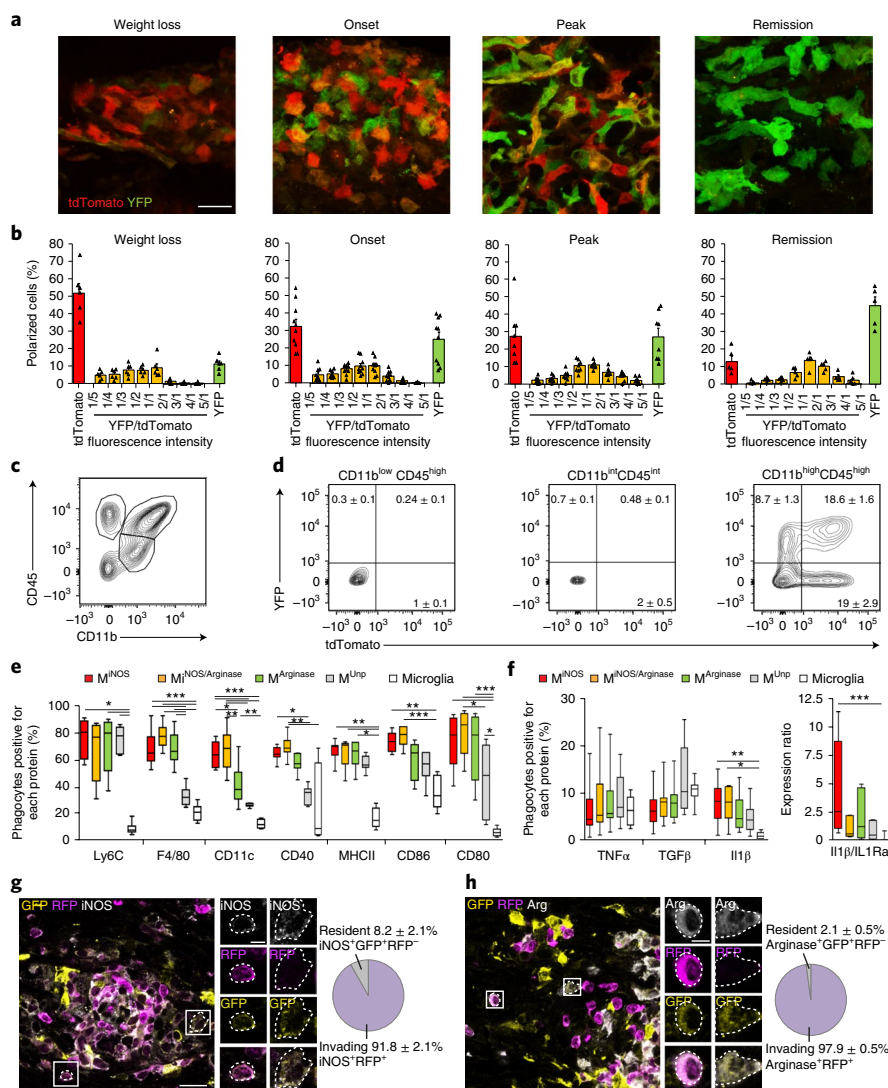


**Fig. 1 | Evolution of phagocyte phenotypes over the course of EAE.** **a, b**, Confocal images of spinal cord lesions (**a**) and quantitative analysis (**b**) of  $M^{iNOS}$ ,  $M^{iNOS/Arginase}$ , and  $M^{Arginase}$  cells at the indicated EAE timepoints in  $iNOS$ -tdTomato-Cre  $\times$  Arginase-YFP mice ( $n=6$  mice at weight loss,  $n=10$  at onset,  $n=8$  at peak,  $n=5$  at remission). Differences over time were analyzed by two-way ANOVA with Bonferroni post hoc correction for  $M^{iNOS}$  and  $M^{Arginase}$  cells only: interaction  $P < 0.0001$ ; for  $M^{iNOS}$ , for weight loss vs. onset ( $*P = 0.0476$ ), for weight loss vs. peak ( $**P = 0.0079$ ), for weight loss vs. remission ( $***P < 0.0001$ ); for  $M^{Arginase}$  cells, for weight loss vs. remission ( $***P = 0.0006$ ). Data are shown as average  $\pm$  s.e.m. with overlaid single data points; slash marks on the x axes represent ratios of background-corrected YFP/tdTomato fluorescence intensities;  $*P < 0.05$ ,  $**P < 0.01$ ,  $***P < 0.001$ . Scale bar,  $20 \mu\text{m}$ . **c, d**, Flow cytometric analysis of reporter expression in CNS-isolated cells from  $iNOS$ -tdTomato-Cre  $\times$  Arginase-YFP mice at peak of disease (average  $\pm$  s.e.m., 3 independent experiments,  $n=9$ ). **e**, Analysis of Ly6C, F4/80, CD11c, CD40, MHC-II, CD86, and CD80 expression in unpolarized ( $M^{Unp}$ ) and polarized  $CD45^{high}CD11b^{high}$  phagocytes and in  $CD45^{int}CD11b^{int}$  microglia isolated at peak of disease (2 independent experiments,  $n=6$  mice). Int, intermediate. **f**, Expression of TNF $\alpha$ , TGF $\beta$ , and IL1 $\beta$  and expression ratio of IL1 $\beta$ /IL1Ra in unpolarized and polarized  $CD45^{high}CD11b^{high}$  phagocytes and  $CD45^{int}CD11b^{int}$  microglia isolated at peak of disease (2 independent experiments,  $n=8$  mice). Data in **e** and **f** are shown as box-and-whiskers (ends of the box represent lower and upper quartiles, median is marked by a vertical line inside the box, whiskers show minimum and maximum values) plots (Kruskal-Wallis with Dunn's post hoc comparisons: Ly6C  $P = 0.006$  ( $M^{Unp}$  vs. microglia  $P = 0.031$ ,  $M^{iNOS}$  vs. microglia  $P = 0.0117$ ,  $M^{Arginase}$  vs. microglia  $P = 0.0229$ ), CD40  $P = 0.0003$  ( $M^{Unp}$  vs.  $M^{iNOS}$   $P = 0.0228$ ,  $M^{Unp}$  vs.  $M^{iNOS/Arginase}$   $P = 0.0017$ ,  $M^{iNOS/Arginase}$  vs. microglia  $P = 0.0084$ ), MHC-II  $P = 0.0005$  ( $M^{iNOS}$  vs. microglia  $P = 0.0023$ ,  $M^{iNOS/Arginase}$  vs. microglia  $P = 0.0016$ ,  $M^{Arginase}$  vs. microglia  $P = 0.01$ ), CD86  $P = 0.0001$  ( $M^{iNOS/Arginase}$  vs. microglia  $P = 0.0005$ ,  $M^{iNOS}$  vs. microglia  $P = 0.0017$ ), TNF $\alpha$   $P = 0.84$ , IL1 $\beta$ /IL1Ra  $P = 0.0023$  ( $M^{iNOS}$  vs. microglia  $P = 0.0008$ ); one-way ANOVA with Bonferroni post hoc correction: F4/80  $P < 0.0001$  (all significant comparisons  $P < 0.0001$ ), CD11c  $P < 0.0001$  ( $M^{Unp}$  vs.  $M^{iNOS}$   $P < 0.0001$ ,  $M^{Unp}$  vs.  $M^{iNOS/Arginase}$   $P < 0.0001$ ,  $M^{Arginase}$  vs.  $M^{iNOS}$   $P = 0.0122$ ,  $M^{iNOS}$  vs.  $M^{iNOS/Arginase}$   $P = 0.0031$ ,  $M^{Arginase}$  vs. microglia  $P = 0.0013$ ,  $M^{iNOS/Arginase}$  vs. microglia  $P < 0.0001$ ,  $M^{iNOS}$  vs. microglia  $P < 0.0001$ ), CD80  $P < 0.0001$  ( $M^{Unp}$  vs.  $M^{iNOS/Arginase}$   $P = 0.0241$ ,  $M^{Arginase}$  vs. microglia  $P < 0.0001$ ,  $M^{iNOS/Arginase}$  vs. microglia  $P < 0.0001$ ,  $M^{iNOS}$  vs. microglia  $P < 0.0001$ ,  $M^{Unp}$  vs. microglia  $P = 0.0158$ ), TGF $\beta$   $P = 0.25$ , IL1 $\beta$   $P = 0.008$  ( $M^{iNOS}$  vs. microglia  $P = 0.009$ ,  $M^{iNOS/Arginase}$  vs. microglia  $P = 0.022$ ). Significant changes are represented as  $*P < 0.05$ ,  $**P < 0.01$ ,  $***P < 0.001$ . **g**, Confocal image (scale bar,  $20 \mu\text{m}$ ; magnified insets,  $5 \mu\text{m}$ ) of a spinal lesion in  $CCR2^{RFP/+} \times CX3CR1^{GFP/+}$  mice at peak of EAE (GFP, yellow; RFP, magenta; iNOS, gray), left, and quantitative analysis of the proportion of resident cells ( $iNOS^+GFP^+RFP^-$ ) and invading cells ( $iNOS^+RFP^+$ ), right. Data are shown as average of expression  $\pm$  s.e.m. ( $n=4$  mice and 516 cells analyzed). **h**, Confocal image (scale bar,  $20 \mu\text{m}$ ; magnified insets,  $5 \mu\text{m}$ ) of spinal cord lesions in  $CCR2^{RFP/+} \times CX3CR1^{GFP/+}$  mice analyzed at peak of EAE (GFP, yellow; RFP, magenta; arginase, gray), left, and quantitative analysis of the proportion of resident cells ( $Arg^+GFP^+RFP^-$ ) and invading cells ( $Arg^+RFP^+$ ), right. Data are shown as average of expression  $\pm$  s.e.m. ( $n=4$  mice and 448 cells analyzed).

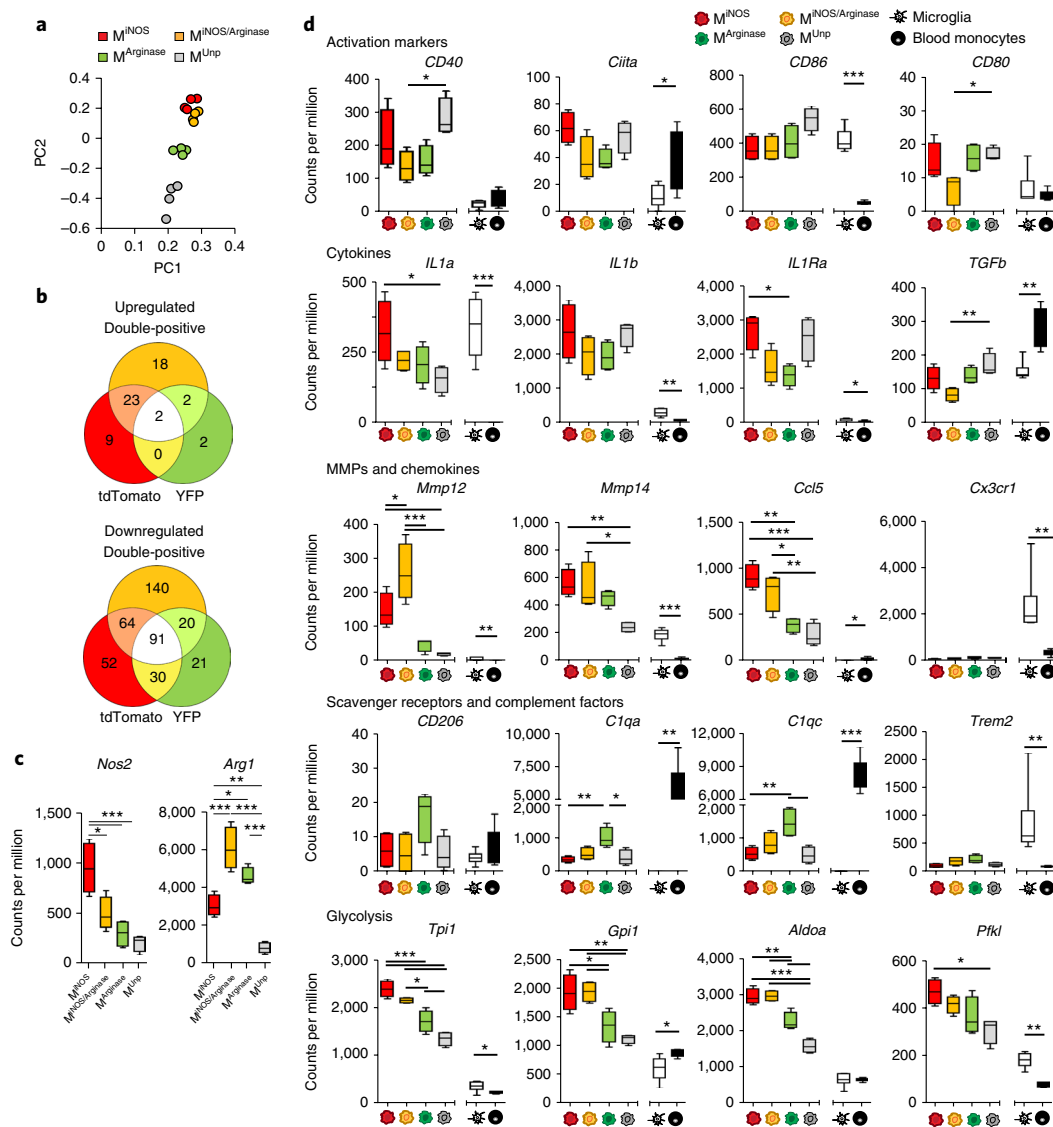


**Fig. 2 | Transcriptional profiles of CNS phagocytes at disease initiation.** **a–c**, RNA sequencing analysis of  $CD45^{\text{high}}CD11b^{\text{high}}CD64^+$  cells isolated from the CNS of  $iNOS$ -tdTomato-Cre  $\times$  Arginase-YFP mice at weight loss ( $n=4$  animals). Shown are **(a)** principal component analysis, **(b)** Venn diagrams of significantly regulated genes in polarized compared to unpolarized cells (see Methods), **(c)** Expression of *Nos2* and *Arg1* shown as box-and-whisker (ends of the box represent lower and upper quartiles, median is marked by a vertical line inside the box, whiskers show minimum and maximum values) plots and analyzed using one-way ANOVA with Bonferroni post hoc corrections, \*  $P < 0.05$ , \*\*  $P < 0.01$ , \*\*\*  $P < 0.001$ . For *Nos2*,  $P=0.0002$  ( $M^{iNOS}$  vs.  $M^{iNOS/Arginase}$   $P=0.0157$ ,  $M^{iNOS}$  vs.  $M^{Arginase}$   $P=0.001$ ,  $M^{iNOS}$  vs.  $M^{Unp}$   $P=0.0003$ ); for *Arg1*  $P < 0.0001$  ( $M^{iNOS}$  vs.  $M^{iNOS/Arginase}$   $P=0.0002$ ,  $M^{iNOS}$  vs.  $M^{Arginase}$   $P=0.0443$ ,  $M^{iNOS}$  vs.  $M^{Unp}$   $P=0.0035$ ,  $M^{iNOS/Arginase}$  vs.  $M^{Unp}$   $P < 0.0001$ ,  $M^{Arginase}$  vs.  $M^{Unp}$   $P < 0.0001$ ). **d**, Count per million (c.p.m.) expression of selected genes from isolated  $CD45^{\text{high}}CD11b^{\text{high}}CD64^+$   $M^{iNOS}$ ,  $M^{iNOS/Arginase}$ ,  $M^{Arginase}$ , and  $M^{Unp}$  isolated from the CNS of  $iNOS$ -tdTomato-Cre  $\times$  Arginase-YFP mice at weight loss ( $n=4$  mice). On the right of each graph, expression of the same transcripts from  $CD45^{\text{int}}CD11b^{\text{int}}$  microglia isolated from the CNS and  $CD45^{\text{high}}CD11b^{\text{high}}CD115^+$  monocytes isolated from the blood of  $iNOS$ -tdTomato-Cre  $\times$  Arginase-YFP mice at weight loss ( $n=6$  mice). Data are presented as box-and-whiskers (ends of the box represent lower and upper quartiles, median is marked by a vertical line inside the box, whiskers show minimum and maximum values) plots. \*  $P < 0.05$ , \*\*  $P < 0.01$ , \*\*\*  $P < 0.001$ ; for the comparisons of  $M^{iNOS}$ ,  $M^{Arginase}$ ,  $M^{iNOS/Arginase}$  and  $M^{Unp}$  cells, all transcripts were analyzed with one-way ANOVA with Bonferroni post hoc correction: for *CD40*,  $P=0.0238$  ( $M^{iNOS/Arginase}$  vs.  $M^{Unp}$   $P=0.0367$ ); *Ccl1a*,  $P=0.0381$ ; *CD86*,  $P=0.0279$ ; *CD80*,  $P=0.0269$  ( $M^{iNOS/Arginase}$  vs.  $M^{Unp}$   $P=0.0414$ ); *Il1a*,  $P=0.039$  ( $M^{iNOS}$  vs.  $M^{Unp}$   $P=0.0376$ ); *Il1b*,  $P=0.18$ ; *Il1Ra*,  $P=0.008$  ( $M^{iNOS}$  vs.  $M^{Arginase}$   $P=0.0208$ ); *TGFb*,  $P=0.008$  ( $M^{iNOS/Arginase}$  vs.  $M^{Unp}$   $P=0.0061$ ); *Mmp12*,  $P < 0.0001$  ( $M^{iNOS/Arginase}$  vs.  $M^{iNOS}$   $P=0.0499$ ,  $M^{iNOS}$  vs.  $M^{Unp}$   $P=0.023$ ,  $M^{iNOS/Arginase}$  vs.  $M^{Arginase}$   $P=0.0004$ ,  $M^{iNOS/Arginase}$  vs.  $M^{Unp}$   $P=0.0001$ ); *Mmp14*,  $P=0.0055$  ( $M^{iNOS}$  vs.  $M^{Unp}$   $P=0.0079$ ,  $M^{iNOS/Arginase}$  vs.  $M^{Unp}$   $P=0.0163$ ); *Ccl5*,  $P < 0.0001$  ( $M^{iNOS}$  vs.  $M^{Arginase}$   $P=0.0012$ ,  $M^{iNOS}$  vs.  $M^{Unp}$   $P=0.0002$ ,  $M^{iNOS/Arginase}$  vs.  $M^{Arginase}$   $P=0.0136$ ,  $M^{iNOS/Arginase}$  vs.  $M^{Unp}$   $P=0.0029$ ); *Cx3cr1*,  $P=0.1$ ; *CD206*,  $P=0.065$ ; *C1qa*,  $P=0.0046$  ( $M^{iNOS}$  vs.  $M^{Arginase}$   $P=0.0073$ ,  $M^{Unp}$  vs.  $M^{Arginase}$   $P=0.0136$ ); *C1qc*,  $P=0.0034$  ( $M^{iNOS}$  vs.  $M^{Arginase}$   $P=0.0084$ ,  $M^{Unp}$  vs.  $M^{Arginase}$   $P=0.0056$ ); *Trem2*,  $P=0.063$ ; *Tpi1*,  $P < 0.0001$  ( $M^{iNOS}$  vs.  $M^{Arginase}$   $P=0.0004$ ,  $M^{iNOS}$  vs.  $M^{Unp}$   $P < 0.0001$ ,  $M^{iNOS/Arginase}$  vs.  $M^{Arginase}$   $P=0.0155$ ,  $M^{iNOS/Arginase}$  vs.  $M^{Unp}$   $P < 0.0001$ ,  $M^{Unp}$  vs.  $M^{Arginase}$   $P=0.046$ ); *Gpi1*,  $P=0.0004$  ( $M^{iNOS}$  vs.  $M^{Arginase}$   $P=0.0213$ ,  $M^{iNOS}$  vs.  $M^{Unp}$   $P=0.002$ ,  $M^{iNOS/Arginase}$  vs.  $M^{Arginase}$   $P=0.0184$ ,  $M^{iNOS/Arginase}$  vs.  $M^{Unp}$   $P=0.0018$ ); *Aldoa*,  $P < 0.0001$  ( $M^{iNOS}$  vs.  $M^{Arginase}$   $P=0.0032$ ,  $M^{iNOS}$  vs.  $M^{Unp}$   $P < 0.0001$ ,  $M^{iNOS/Arginase}$  vs.  $M^{Arginase}$   $P=0.0025$ ,  $M^{iNOS/Arginase}$  vs.  $M^{Unp}$   $P < 0.0001$ ,  $M^{Unp}$  vs.  $M^{Arginase}$   $P=0.003$ ); *Pfkf*,  $P=0.011$  ( $M^{iNOS}$  vs.  $M^{Unp}$   $P=0.0114$ ). For the comparisons of blood monocytes and microglia, *CD40* ( $P=0.81$ ), *CD80* ( $P=0.309$ ), *TGFb* ( $P=0.0022$ ), *Mmp12* ( $P=0.0022$ ), *Cx3cr1* ( $P=0.0022$ ), *C1qa* ( $P=0.0022$ ), *Trem2* ( $P=0.0022$ ), and *Pfkf* ( $P=0.0022$ ) were analyzed with Mann-Whitney tests; other transcripts were analyzed using unpaired, two-sided *t* tests: *Ccl1a*,  $P=0.0334$ ; *CD86*,  $P < 0.0001$ ; *Il1a*,  $P < 0.0001$ ; *Il1b*,  $P=0.001$ ; *Il1Ra*,  $P=0.0412$ ; *Mmp14*,  $P < 0.0001$ ; *Ccl5*,  $P=0.0181$ ; *CD206*,  $P=0.124$ ; *C1qc*,  $P < 0.0001$ ; *Tpi1*,  $P=0.017$ ; *Gpi1*,  $P=0.0126$ ; and *Aldoa*,  $P=0.989$ . MMPs, matrix metalloproteinases.



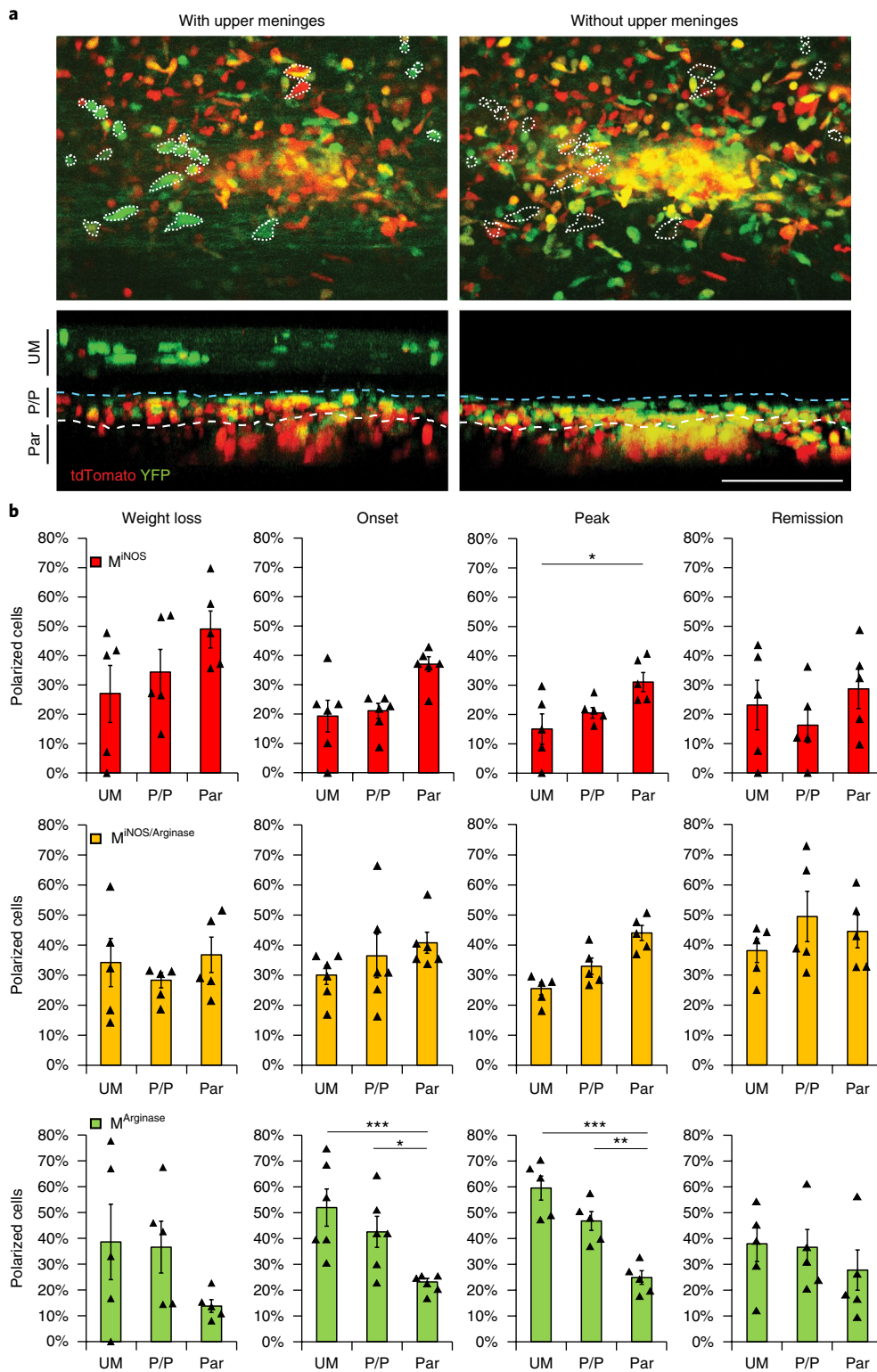


**Fig. 4 | Local specification of phagocyte phenotypes in the spinal cord. a**, In vivo images of the spinal cord of iNOS-tdTomato-Cre x Arginase-YFP mice at EAE onset before (left) and after (right) removal of upper meninges. Lower panels illustrate lateral projection highlighting the different CNS microenvironments (UM, upper meninges; P/P, pia-parenchyma interface; par, parenchyma). Dashed cell contours (above) indicate UM cells; dashed lines (below) indicate upper (cyan) and lower (white) P/P limits. Scale bar, 90  $\mu$ m. **b**, Quantitative analysis of polarized cell percentage in the spinal cord of iNOS-tdTomato-Cre x Arginase-YFP mice at the indicated EAE timepoints ( $n = 5$  mice for weight loss, 6 mice for onset, 5 mice for peak, 5 mice for remission). Differences over time were analyzed by two-way ANOVA with Bonferroni post hoc correction only for  $M^{iNOS}$  and  $M^{Arginase}$  cells. At weight loss: interaction  $P = 0.0443$ ; at onset: interaction  $P < 0.0001$ , reporter  $P = 0.0019$ ; at peak: interaction and reporter  $P < 0.0001$ . At onset for  $M^{Arginase}$  cells: parenchyma vs. meninges  $P = 0.0009$ , parenchyma vs. P/P  $P = 0.0401$ ; at peak for  $M^{iNOS}$  cells: parenchyma vs. meninges  $P = 0.0322$ , at peak for  $M^{Arginase}$  cells: parenchyma vs. meninges  $P < 0.0001$ , parenchyma vs. P/P  $P = 0.0022$ . Data are shown as average  $\pm$  s.e.m. with overlaid single data points; \* $P < 0.05$ , \*\* $P < 0.01$ , \*\*\* $P < 0.001$ .

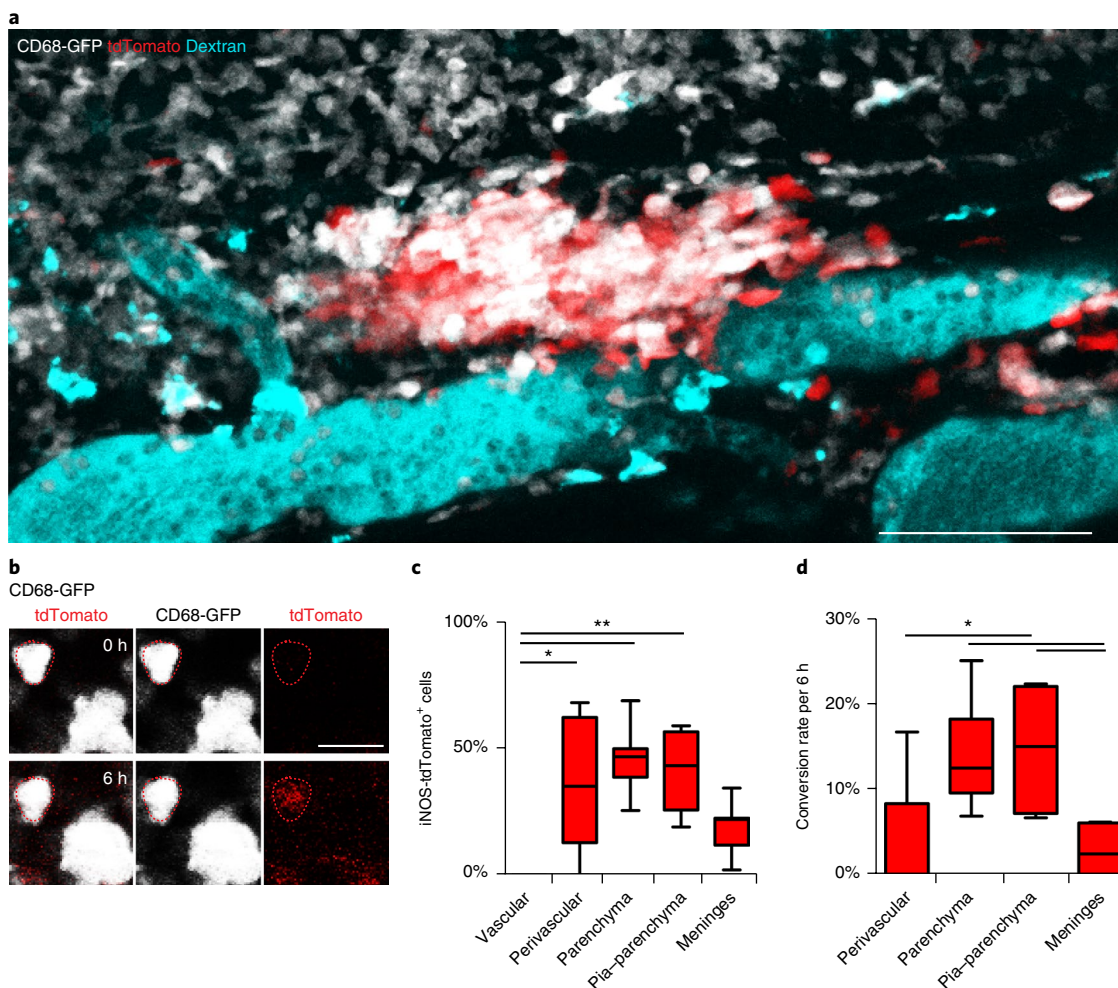


**Fig. 5 | Initial polarization of  $M^{iNOS}$  cells in spinal lesions. **a, b****, In vivo image (**a**) of a spinal cord lesion (scale bar, 100  $\mu\text{m}$ ) and (**b**) in vivo time-lapse imaging (scale bar, 20  $\mu\text{m}$ ) of iNOS-tdTomato-Cre  $\times$  CD68-GFP mice at EAE onset. Dashed cell contours outline an unpolarized GFP<sup>+</sup> cell becoming GFP<sup>+</sup>  $M^{iNOS}$  after 6 h. **c, d**, Quantitative analysis of the proportion of (**c**) GFP<sup>+</sup>  $M^{iNOS}$  (red) and unpolarized GFP<sup>+</sup> cells (gray) and (**d**) conversion rate of unpolarized GFP<sup>+</sup> (gray) to GFP<sup>+</sup>  $M^{iNOS}$  (red) cells in the different spinal cord compartments of iNOS-tdTomato-Cre  $\times$  CD68-GFP mice at EAE onset ( $n = 7$  mice). Data are shown as box-and-whiskers (ends of the box represent lower and upper quartiles, median is marked by a vertical line inside the box, whiskers show minimum and maximum values) plots. \* $P < 0.05$ , \*\* $P < 0.01$ , \*\*\* $P < 0.001$ ; Kruskal-Wallis tests with Dunn's post hoc comparisons: (**c**)  $P = 0.0006$ ; vascular vs. perivascular  $P = 0.0266$ , vascular vs. parenchyma  $P = 0.0010$ , vascular vs. P/P  $P = 0.0069$ ; (**d**)  $P = 0.0019$ ; P/P vs. perivascular  $P = 0.0495$ , meninges vs. parenchyma  $P = 0.0311$ , P/P vs. meninges  $P = 0.0295$ .

in the meninges or the perivascular space rarely initiated tdTomato expression (Fig. 5d). Taken together, these results suggest that during the formation of neuroinflammatory lesions, phagocytes enter the CNS parenchyma as unpolarized cells and locally encounter signals from, for example, pioneering T cells<sup>29</sup> that initiate their proinflammatory polarization.

**Individual phagocytes shift their phenotype in response to CNS-derived signals.** After the initial  $M^{iNOS}$  polarization was established, the overall phagocyte population in spinal EAE lesions progressively shifted to an  $M^{Arginase}$  phenotype over the course of the disease. Such a population shift could be achieved in more than one way. Potentially,  $M^{iNOS}$  cells could die over time or leave the CNS while being replaced by the invasion of  $M^{Arginase}$  (or  $M^{iNOS/Arginase}$ ) cells. Alternatively, individual  $M^{iNOS}$  cells could switch their polarization over time, presumably first to an  $M^{iNOS/Arginase}$  and later to an  $M^{Arginase}$  phenotype. Therefore, to distinguish between these possibilities, we performed different sets of experiments.

First, we asked whether individual phagocytes are capable of switching their phenotype in inflammatory CNS lesions. To answer

this question, we performed time-lapse in vivo imaging of individual phagocytes during 6-h segments at different stages of the formation and resolution of neuroinflammatory lesions (Fig. 6a–d and Supplementary Video 3; details in Methods). Tracking several thousands of cells over time revealed that single phagocytes can indeed adapt their phenotype in the CNS and that this adaptation follows an  $M^{iNOS} \rightarrow M^{iNOS/Arginase} \rightarrow M^{Arginase}$  sequence. While the highest rates of  $M^{iNOS}$  to  $M^{iNOS/Arginase}$  conversions were observed in initial lesions (at the weight loss stage), the rate of  $M^{iNOS/Arginase}$  to  $M^{Arginase}$  conversions increased over time and was highest during lesion resolution (at 7 d after EAE onset; Fig. 6d). In contrast, conversions in the opposite direction were rarely, if ever, observed (one  $M^{Arginase}$  to  $M^{iNOS/Arginase}$  conversion observed for 784  $M^{Arginase}$  cells monitored and no  $M^{iNOS/Arginase}$  to  $M^{iNOS}$  conversion observed for 1,439  $M^{iNOS/Arginase}$  cells monitored). Like the initial  $M^{iNOS}$  polarization, this switch of the phagocyte phenotype happened most frequently in the parenchyma and at the pia–parenchyma border (Supplementary Fig. 9). Taken together, these experiments demonstrate in real time that individual phagocytes can change their phenotype in the CNS and indicate that this adaptation occurs along the  $M^{iNOS} - M^{iNOS/Arginase} - M^{Arginase}$  axis.

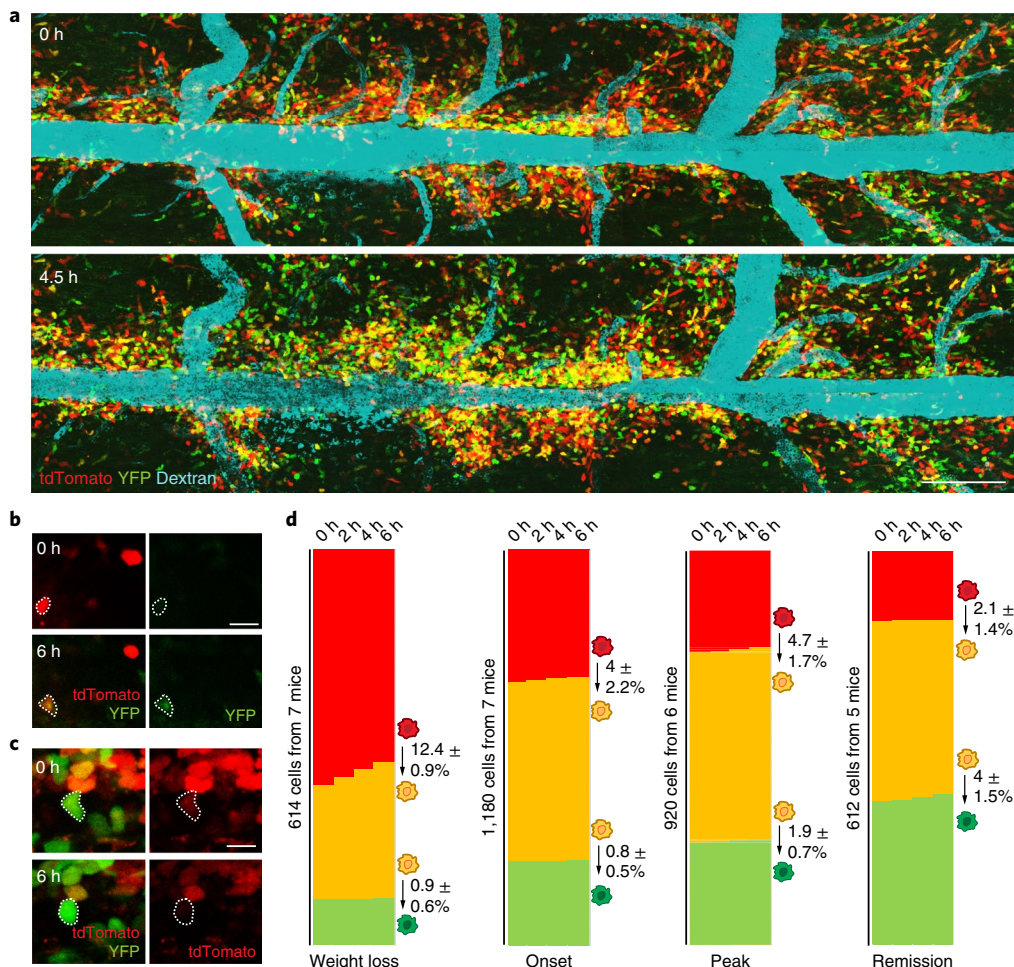


**Fig. 6 | Single-cell tracking of phagocyte phenotypes in vivo.** **a–c**, Time-lapse in vivo imaging of the spinal cord of iNOS-tdTomato-Cre x Arginase-YFP mice (**a**) at peak of EAE (scale bar, 200  $\mu$ m); (**b**) at weight loss, illustrating an  $M^{iNOS}$  (top) becoming an  $M^{iNOS/Arginase}$  cell (bottom; scale bar, 20  $\mu$ m); and (**c**) at disease peak, illustrating an  $M^{iNOS/Arginase}$  (top) becoming an  $M^{Arginase}$  cell (bottom; scale bar, 5  $\mu$ m). **d**, Quantitative analysis of individual phagocyte phenotypes imaged in vivo in spinal lesions of iNOS-tdTomato-Cre x Arginase-YFP mice. Shown are proportions of  $M^{iNOS}$  cells switching to  $M^{iNOS/Arginase}$  (top) and of  $M^{iNOS/Arginase}$  cells switching to  $M^{Arginase}$  (bottom) over 6 h (cells analyzed: weight loss  $n = 614$  cells from 7 mice; onset  $n = 1,180$  cells from 7 mice; peak  $n = 920$  cells from 6 mice; remission  $n = 612$  cells from 5 mice). Conversion rates shown next to the graphs are calculated per mouse and shown as average  $\pm$  s.e.m.

Next, we set out to determine whether a true intermediate  $M^{iNOS/Arginase}$  phagocyte phenotype exists in the inflamed CNS. Even if a large fraction of phagocytes are positive for both tdTomato and YFP reporter proteins, this does not necessarily imply that the promoters driving the expression of these genes are indeed active at the same time. This is of particular relevance for the iNOS-tdTomato-Cre mouse line, in which the expression of a protein with a very short half-life (iNOS<sup>30</sup>) is monitored by the expression of a much more stable fluorescent protein (tdTomato). To directly monitor the activity of iNOS and arginase promoters in CNS phagocytes, we thus developed an in vivo bleaching approach. Here we recorded fluorescence levels in an EAE lesion before using a spatially restricted exposure to higher laser intensities to bleach about 80% of the tdTomato and about 50% of the YFP fluorescence in a defined group of phagocytes. In vivo time-lapse imaging then allowed us to determine fluorescence recovery in bleached phagocytes and relate it to fluorescence changes in cells located in the same imaging plane but outside of the bleaching area (Fig. 7a). Around 80% of  $M^{iNOS}$  and  $M^{Arginase}$  showed an active promoter at the beginning of EAE, while this proportion dropped to around 50% at later stages (Fig. 7b). Notably, many  $M^{iNOS/Arginase}$  cells actively expressed both genes, thus confirming that an intermediate phenotype exists in vivo (Fig. 7c,d).

Next, we estimated the relative contribution of phenotype switches to the evolution of the entire phagocyte population in neuroinflammatory lesions. We made use of the Cre recombinase that iNOS-tdTomato-Cre mice express together with the tdTomato reporter, and crossed these mice with a Rosa26-Stp-fl-YFP mouse line, in which YFP expression is selectively induced in Cre-expressing cells. Arginase-specific immunostaining then allowed us to track the origin of  $M^{Arginase}$  cells in inflammatory CNS lesions: those cells that co-express arginase and YFP have undergone a phenotype switch, while those that express arginase but no YFP have not. An important prerequisite for this approach is that phagocytes in the blood stream not only did not express iNOS at this time (Supplementary Fig. 8a,b), but had never expressed iNOS before. We determined that this was indeed the case by flow cytometric analysis of peripheral blood from iNOS-tdTomato-Cre x Rosa26-Stp-fl-YFP mice (Supplementary Fig. 8c,d). Furthermore, we confirmed the efficiency of the Cre expression in iNOS-tdTomato mice by analyzing the presence of YFP in those phagocytes that currently expressed tdTomato. Such co-expression was indeed observed in  $84.7 \pm 3.7\%$  of all tdTomato<sup>+</sup> CNS phagocytes ( $n = 344$  phagocytes from 4 mice). Having established the assay, we then used this strategy to determine how the  $M^{Arginase}$  phenotype is acquired in spinal

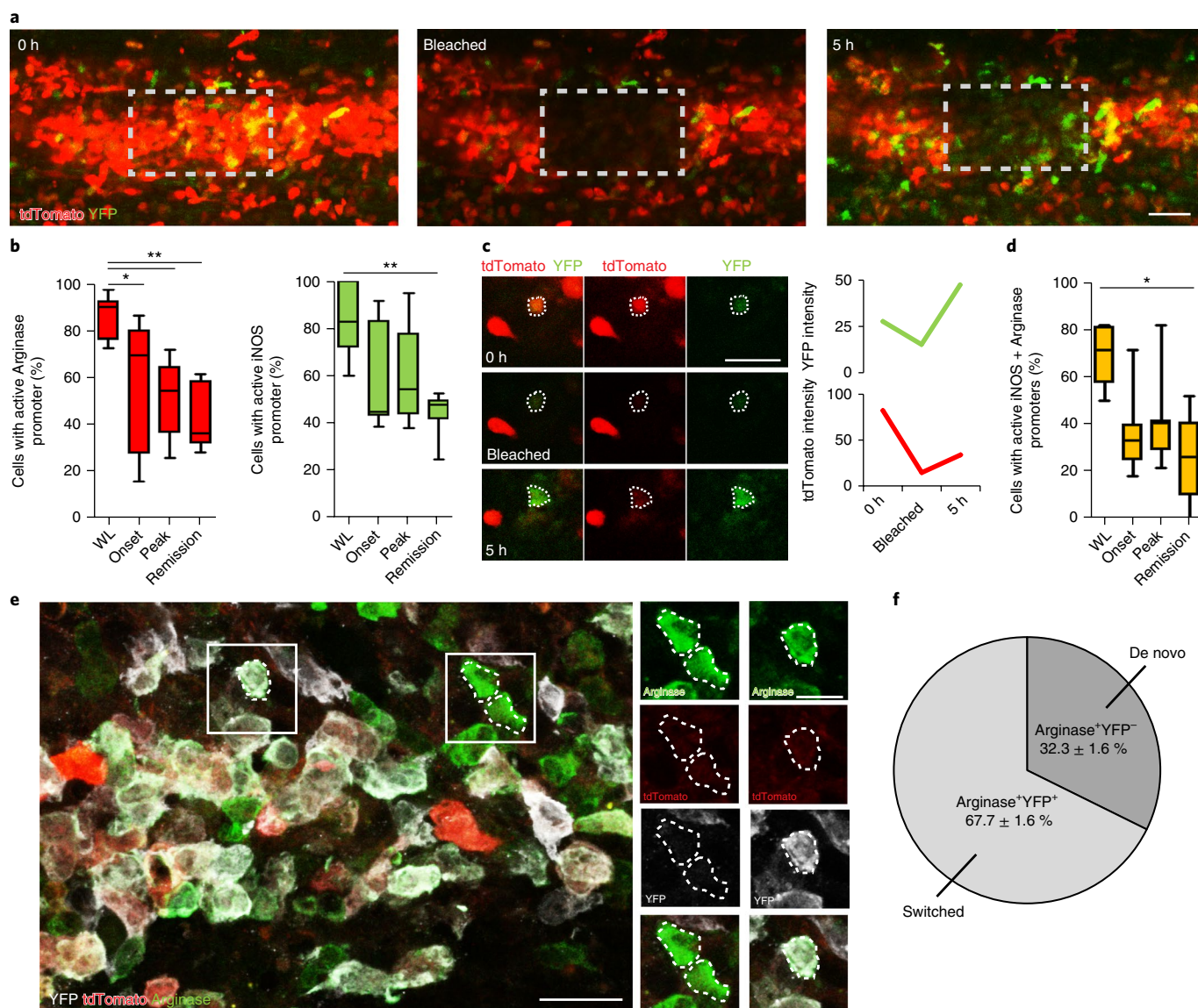


**Fig. 7 | Dynamic and fate tracking analysis of phenotype conversion in the inflamed spinal cord. a–d**, Analysis of iNOS and Arginase-1 promoter activity by *in vivo* imaging of iNOS-tdTomato-Cre × Arginase-YFP mice at different EAE timepoints. **(a)** *In vivo* images at EAE onset before bleaching (left), after bleaching (center), and 5 h later (right). Scale bar, 40  $\mu$ m. **(b)** Percentage of M<sup>iNOS</sup> (left) and M<sup>Arginase</sup> (right) cells with active promoter, box-and-whiskers (ends of the box represent lower and upper quartiles, median is marked by a vertical line inside the box, whiskers show minimum and maximum values) plots, \* $P < 0.05$ , \*\* $P < 0.01$  (M<sup>iNOS</sup> cells  $P = 0.0011$  (weight loss (WL) vs. onset  $P = 0.0349$ , WL vs. peak  $P = 0.0078$ , WL vs. remission  $P = 0.0011$ ), one-way ANOVA with Bonferroni post hoc correction test; M<sup>Arginase</sup> cells  $P = 0.013$  (WL vs. remission  $P = 0.0092$ ), Kruskal-Wallis with Dunn's post hoc comparisons;  $n = 7$  mice). **(c)** *In vivo* time-lapse and fluorescent intensities of an M<sup>iNOS/Arginase</sup> cell (outlined) before and after bleaching; data representative of 7 independent experiments. Scale bar, 25  $\mu$ m. **(d)** Percentage of M<sup>iNOS/Arginase</sup> cells with active iNOS and Arginase-1 promoters ( $n = 7$  mice). Data are shown as box-and-whiskers (ends of the box represent lower and upper quartiles, median is marked by a vertical line inside the box, whiskers show minimum and maximum values) plots, \* $P < 0.05$  (Kruskal-Wallis with Dunn's post hoc comparisons  $P = 0.019$  (WL vs. remission  $P = 0.0192$ )). **e**, Confocal image and magnified insets, showing de novo YFP<sup>-</sup> M<sup>Arginase</sup> cells, left, and a switched YFP<sup>positive</sup> M<sup>Arginase</sup> cell, right. Scale bar, 20  $\mu$ m; insets, 10  $\mu$ m. **f**, Quantitative analysis of the proportion of de novo YFP<sup>-</sup> M<sup>Arginase</sup> and switched YFP<sup>+</sup> M<sup>Arginase</sup> cells in spinal lesions of iNOS-tdTomato-Cre × Rosa26-Stp-fl-YFP mice ( $n = 4$  mice) analyzed 1 or 2 d after EAE onset. Data are shown as average  $\pm$  s.e.m.

lesions 2 d after onset of EAE. Our results revealed that about 2/3 of all M<sup>Arginase</sup> cells were derived from former M<sup>iNOS</sup> cells, while about 1/3 arose de novo (Fig. 7e,f).

Finally, we wanted to understand how this local phenotype shift of CNS phagocytes is induced. To address whether the phenotype shift is regulated in an autocrine or paracrine manner, we isolated bone marrow-derived macrophages from iNOS-tdTomato-Cre × Arginase-YFP mice, polarized them to an M<sup>iNOS</sup> phenotype by incubation with LPS and IFN $\gamma$  for 48 h, changed the medium,

and then followed the phenotype resolution over the next 3 d. Our results showed that M<sup>iNOS</sup> cells in the absence of exogenous mediators lost tdTomato expression without shifting to YFP expression, while such an expression shift could be induced by incubation with mediators of alternative phagocyte activation such as IL4 and IL13 (Fig. 8a–f). Together, these results indicate that the M<sup>iNOS</sup>-to-M<sup>Arginase</sup> shift is not a default pathway along which M<sup>iNOS</sup> activation is resolved and argues that paracrine signals are required for the phenotype shift. To resolve the nature of such paracrine signals,

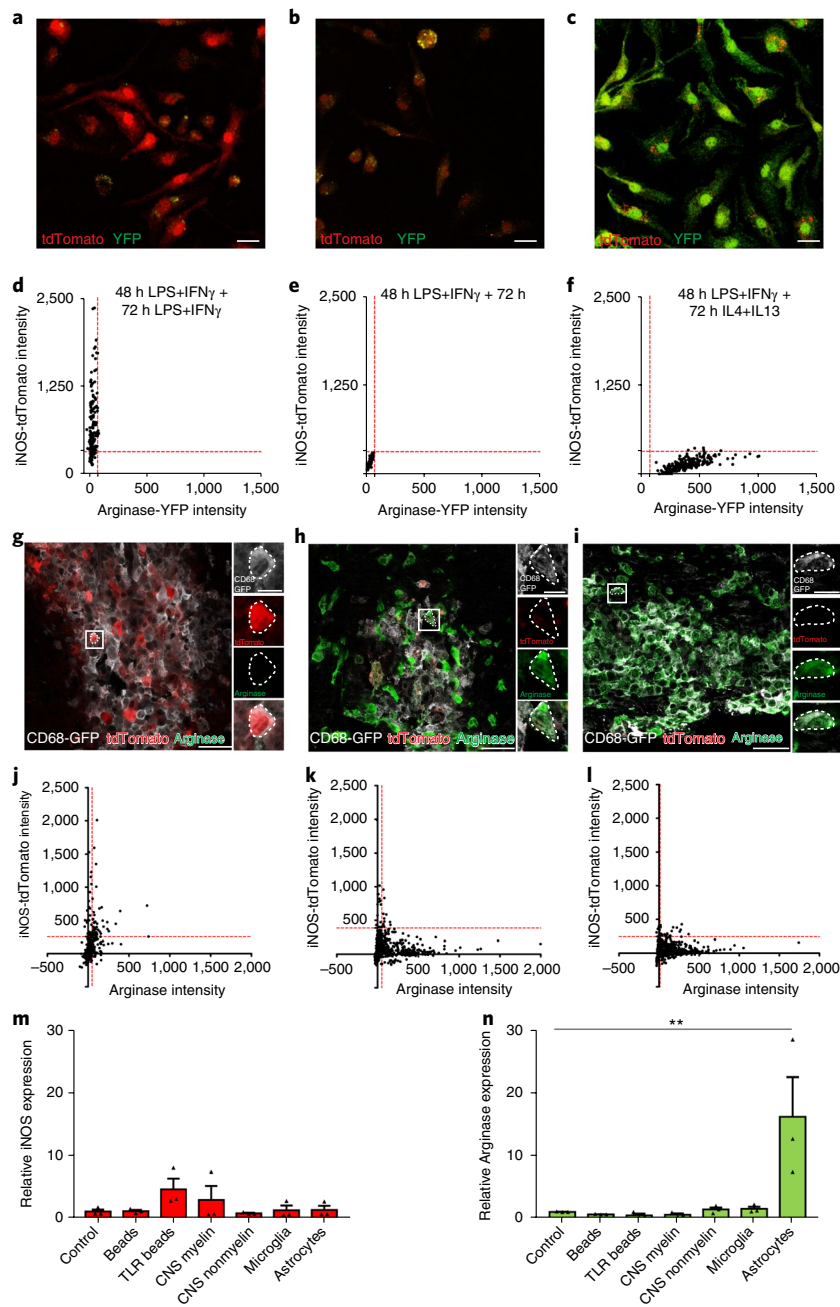


**Fig. 8 | Evolution of phagocyte phenotypes following in vitro polarization, in vivo spinal cord cell injections, and exposure to defined CNS fractions and cell types.** **a–c**, Confocal images of iNOS-tdTomato and Arginase-YFP immunostaining. Scale bar, 20  $\mu\text{m}$ . **d–f**, Respective quantifications of bone marrow-derived macrophages isolated from iNOS-tdTomato-Cre  $\times$  Arginase-YFP mice in culture for **(a,d)** 48 h in LPS + IFN $\gamma$  followed by washing and 72 h in LPS + IFN $\gamma$  (81.1  $\pm$  10.1% of cells are M<sup>iNOS</sup>,  $n$  = 162 cells analyzed); **(b,e)** 48 h in LPS + IFN $\gamma$  followed by washing and 72 h without polarization (all cells are unpolarized,  $n$  = 201 cells analyzed); and **(c,f)** 48 h in LPS + IFN $\gamma$  followed by washing and 72 h in IL4 + IL13 (97.9  $\pm$  0.1% of cells are M<sup>Arginase</sup>,  $n$  = 234 cells analyzed). **g–i**, Confocal images of bone marrow-derived macrophages isolated from iNOS-tdTomato-Cre  $\times$  CD68-GFP mice, polarized in vitro for 48 h toward M<sup>iNOS</sup> with LPS + IFN $\gamma$ , and analyzed at **(g)** 24 h and at **(h)** 72 h after injection into the spinal cord of a healthy C57BL/6 mouse and at **(i)** 72 h after injection into the spinal cord of a C57BL/6 mouse at onset of EAE (CD68-GFP, gray; iNOS-tdTomato, red; Arginase co-staining, green). Scale bar, 40  $\mu\text{m}$ ; magnified insets, 10  $\mu\text{m}$ . **j–l**, Quantifications of iNOS-tdTomato and Arginase intensities in transferred CD68-GFP<sup>+</sup> macrophages at **(j)** 24 h after injection in healthy mice ( $n$  = 5 mice; average  $\pm$  s.e.m. of polarized cells: 37.7  $\pm$  12.4% M<sup>iNOS</sup>, 29.4  $\pm$  8.7% M<sup>iNOS/Arginase</sup>, 32.8  $\pm$  10.2% M<sup>Arginase</sup>; 449 cells analyzed), **(k)** 72 h after injection in healthy mice ( $n$  = 5 mice; 20.6  $\pm$  15.8% of all polarized cells are M<sup>iNOS</sup>, 5.7  $\pm$  3.3% are M<sup>iNOS/Arginase</sup>, 73.7  $\pm$  18.6% are M<sup>Arginase</sup>; 780 cells analyzed) and **(l)** 72 h after injection in mice at onset of EAE ( $n$  = 4 mice; average  $\pm$  s.e.m. of polarized cells: 3.7  $\pm$  2.1% M<sup>iNOS</sup>, 4.4  $\pm$  2.8% M<sup>iNOS/Arginase</sup>, 91.9  $\pm$  4.1% M<sup>Arginase</sup>; 714 cells analyzed). **m,n**, Quantitative PCR analysis of iNOS (**m**) and Arginase (**n**) transcription in bone marrow-derived macrophages polarized in vitro for 48 h toward M<sup>iNOS</sup> with LPS + IFN $\gamma$  and analyzed at 24 h after culture with medium only (control), latex microspheres (beads), zymosan-coupled bioparticles that stimulate TLR signaling (TLR beads), myelin and nonmyelin fractions of the CNS, or after transwell cultures with isolated microglia cells (microglia) or astrocytes (astrocytes). Data from 3 experiments (with each sample run as a duplicate) are shown as individual values and as average  $\pm$  s.e.m. (\*\*  $P$  < 0.01; one-way ANOVA with Bonferroni post hoc correction vs. control,  $P$  = 0.2522 for **(m)**,  $P$  = 0.0033 (astrocytes vs. control 0.0033) for **(n)**).

we next transferred  $M^{iNOS}$ -polarized bone marrow-derived macrophages isolated from  $iNOS$ -tdTomato-Cre $\times$ CD68-GFP mice with a finely drawn glass capillary into the spinal cord of healthy mice or mice at the onset of EAE. In both cases we observed that many injected (GFP<sup>+</sup>) cells shifted to an  $M^{Arginase}$  phenotype 72 h after transfer (Fig. 8g–l), indicating that signals derived from the CNS environment are sufficient to induce a phenotype shift *in vivo*. This conclusion is further supported by our finding that phagocytes in a spinal cord injury model show robust induction of Arginase expression 72 h after injury (Supplementary Fig. 10). There are several possibilities for how the CNS environment could trigger such a phenotype shift. For example, it has been shown that phagocytosis of tissue debris and particularly of CNS myelin can affect cell phenotype<sup>16</sup>. However, neither incubation of  $M^{iNOS}$  polarized cells with uncoupled or zymosan-coupled beads (which induce phagocytosis) nor incubation with purified myelin or with purified CNS tissue depleted of myelin resulted in increased arginase expression (Fig. 8m,n). Another possibility is that signals derived from CNS resident cells, such as microglia or astrocytes, induce the phenotype adaptation. To test this, we isolated microglial cells and astrocytes from the CNS<sup>31</sup> and used a transwell system to expose  $M^{iNOS}$ -polarized macrophages to signals released by these cell types. Indeed, we observed that  $M^{iNOS}$  phagocytes exposed to astrocyte mediators, but not those exposed to microglial mediators, showed a ~15-fold increase of arginase transcription (Fig. 8m,n). Taken together, our work shows that  $M^{iNOS}$  phagocytes adapt their phenotype as inflammatory CNS lesions evolve toward remission and that signals derived from CNS environment, including mediators released from astrocytes, can instruct this phenotype shift.

## Discussion

Our study provides a temporally and spatially resolved view of phagocyte phenotype evolution during the formation and resolution of neuroinflammatory lesions. One of the conclusions emerging from this work is that the local microenvironment is critical in shaping the phagocyte response. Phagocytes that enter from the blood stream acquire their initial polarization only after spinal cord entry, and the nature of this polarization critically depends on the compartment they enter. While phagocytes in the spinal cord parenchyma predominantly show an  $M^{iNOS}$  polarization at the initial stages of lesion formation, phagocytes in the meninges often display an  $M^{Arginase}$  phenotype. The latter is reminiscent of the anti-inflammatory phenotype of myeloid cells in the meninges that has been described to influence learning and memory under homeostatic conditions<sup>32</sup>. The distinct phenotype of phagocytes in the meninges is also of interest when considering the crucial role the meningeal compartment plays in immune cell trafficking and lymphatic drainage in general<sup>33,34</sup>, as well as considering the meninges specifically as a site of T cell–phagocyte interactions during neuroinflammation<sup>29</sup>. If and how the different phagocyte phenotypes in meningeal and parenchymal compartments help to shape the local T cell responses (and vice versa) will be interesting to explore. Such a reciprocal adaptation is likely to occur, as differentially polarized phagocytes can drive distinct T cell responses, and T cell-derived cytokines in turn influence phagocyte polarizations.

The assumption that mediators released from infiltrating immune cells play an important role in the initial polarization of mononuclear phagocytes after CNS entry is further supported by our findings that resting microglia cells, as well as meningeal and perivascular macrophages, do not show reporter-protein expression in the healthy CNS. While  $iNOS$  and the corresponding tdTomato expression can, in principle, be triggered in microglia cells by intracerebral injection of LPS and IFN- $\gamma$ <sup>20</sup>, few microglia cells become polarized during EAE. The vast majority of polarized cells enter from the blood stream, carry surface markers that suggest that they are predominantly derived from inflammatory monocytes<sup>35</sup>, and

are labeled in CCR2<sup>RFP/WT</sup> mice<sup>22</sup>. These data are in line with previous reports that identified infiltrating phagocytes as critical drivers of EAE initiation and progression<sup>7</sup>.

A more comprehensive analysis of their molecular make up showed that a number of differentially expressed genes and proteins characterize the  $M^{iNOS}$ ,  $M^{iNOS/Arginase}$ , and  $M^{Arginase}$  phenotypes that these cells acquire in the inflamed spinal cord. Some of these are similar to molecular changes observed in classical macrophage polarization experiments *in vitro*, as both transcriptional and proteomic analyses indicated that CNS phagocyte phenotypes differed in their mode of ATP generation, with  $M^{iNOS}$  cells upregulating glycolysis and  $M^{Arginase}$  cells relying more on oxidative phosphorylation. These findings are in line with reports showing that mediators that induce proinflammatory phagocyte polarization, such as LPS and IFN- $\gamma$ , inhibit mitochondrial oxidative respiration and favor glycolysis. Notably, these distinct metabolic states can directly impact phagocyte function, as oxidative phosphorylation supports the expression of M2-associated surface receptors, while the increased mitochondrial membrane potential that results from glycolytic ATP production potentiates proinflammatory phagocyte actions<sup>15,36,37</sup>. Overall, however, many of the classical genes associated with distinct proinflammatory (M1) and anti-inflammatory (M2) phenotypes in cell culture experiments did not appear to be differentially regulated *in vivo*, reinforcing the view that CNS phenotypes of phagocytes are quite different from the M1–M2 dichotomy observed *in vitro* in response to defined activation protocols<sup>38</sup>. This assessment is also supported by our observation that a large fraction of the polarized phagocytes in EAE showed an intermediate phenotype expressing both  $iNOS$  and arginase at the same time. These data are further in line with a number of previous studies showing that phagocytes can express combinations of classical M1 and M2 markers *in vivo*<sup>39,40</sup>. Together, our findings are consistent with the existence of a rather continuous spectrum of phagocyte phenotypes, along which phagocytes can move depending on cues they received from the lesion environment<sup>41</sup>.

At least in EAE, the movement of the phagocyte population along this spectrum appears to be exclusively unidirectional. Initial lesions are dominated by  $M^{iNOS}$  phagocytes, which over time are replaced by  $M^{iNOS/Arginase}$  and ultimately by  $M^{Arginase}$  phagocytes. That the dominant phenotype of the phagocyte population can evolve over time has been observed before both in the injured or inflamed CNS<sup>42–44</sup>, as well as in peripheral tissues that respond to insults or infection<sup>45</sup>. How this phenotypic evolution is achieved on the cellular level, however, is still under debate. While classical concepts favor a sequential infiltration of differentially polarized populations<sup>17,45,46</sup>, some reports have suggested that a phenotype change can also occur locally (for example, in injured skeletal muscle and inflamed joints<sup>47,48</sup>). Here we used spinal *in vivo* imaging to visualize the phenotype of individual phagocytes and track their changes over time, providing direct evidence that phagocytes can switch their polarization in the inflamed spinal cord. This phenotype switch was likely initiated very early after tissue entry, as even  $M^{iNOS}$  phagocytes sorted from initial lesions had increased arginase mRNA expression (Fig. 2c). The signals that induced this phenotype shift appeared to be provided by the local CNS environment, as  $M^{iNOS}$  cells injected into healthy or inflamed spinal cord shifted their phenotype toward  $M^{Arginase}$  within a few days. These findings highlight the tight regulation of immune reactions in the CNS and suggest that endogenous safeguards are in place that immediately attempt to curb inflammatory CNS damage. Astrocytes appear to be an important cellular component of such CNS safeguards, as they provide soluble signals that induce arginase expression in  $M^{iNOS}$  cells. A key role for astrocyte-derived signals in this process is in line with recent reports that identify reciprocal signaling networks between astrocytes and phagocytes as central regulatory elements of CNS inflammation<sup>49,50</sup>.

Indeed, our fate-tracking analysis showed that such local phenotype switches in the CNS are a major contributor to the transformation of the phagocyte population that parallels the formation and resolution of neuroinflammatory lesions.

These results also have implications for the way we think about targeting phagocyte actions in inflammatory CNS disease like MS. For example, our findings suggest that the initial proinflammatory polarization of phagocytes needs to be prevented rather than reversed, considering that the latter happens endogenously shortly after the cells enter the CNS. Furthermore, the timing of interventions, at least of those that aim to block overall phagocyte infiltration or activation, is crucial. While such interventions are likely beneficial during the formation of lesions, the same strategies may have opposing effects during lesion resolution, when anti-inflammatory phagocytes dominate the infiltrate. Expanding our understanding of how phagocyte phenotypes evolve in vivo can thus help to better define both the therapeutic opportunities and the limitations of targeting phagocyte actions in vivo.

## Methods

Methods, including statements of data availability and any associated accession codes and references, are available at <https://doi.org/10.1038/s41593-018-0212-3>.

Received: 2 May 2018; Accepted: 29 June 2018;

Published online: 20 August 2018

## References

- Dendrou, C. A., Fugger, L. & Friese, M. A. Immunopathology of multiple sclerosis. *Nat. Rev. Immunol.* **15**, 545–558 (2015).
- Mishra, M. K. & Yong, V. W. Myeloid cells - targets of medication in multiple sclerosis. *Nat. Rev. Neurol.* **12**, 539–551 (2016).
- Henderson, A. P., Barnett, M. H., Parratt, J. D. & Prineas, J. W. Multiple sclerosis: distribution of inflammatory cells in newly forming lesions. *Ann. Neurol.* **66**, 739–753 (2009).
- Bitsch, A., Schuchardt, J., Bunkowski, S., Kuhlmann, T. & Brück, W. Acute axonal injury in multiple sclerosis. Correlation with demyelination and inflammation. *Brain* **123**, 1174–1183 (2000).
- Lucchinetti, C. et al. Heterogeneity of multiple sclerosis lesions: implications for the pathogenesis of demyelination. *Ann. Neurol.* **47**, 707–717 (2000).
- Huitinga, I., van Rooijen, N., de Groot, C. J., Uitdehaag, B. M. & Dijkstra, C. D. Suppression of experimental allergic encephalomyelitis in Lewis rats after elimination of macrophages. *J. Exp. Med.* **172**, 1025–1033 (1990).
- Ajami, B., Bennett, J. L., Krieger, C., McNagny, K. M. & Rossi, F. M. Infiltrating monocytes trigger EAE progression, but do not contribute to the resident microglia pool. *Nat. Neurosci.* **14**, 1142–1149 (2011).
- Goldmann, T. et al. A new type of microglia gene targeting shows TAK1 to be pivotal in CNS autoimmune inflammation. *Nat. Neurosci.* **16**, 1618–1626 (2013).
- Ryu, J. K. et al. Blood coagulation protein fibrinogen promotes autoimmunity and demyelination via chemokine release and antigen presentation. *Nat. Commun.* **6**, 8164 (2015).
- Spath, S. et al. Dysregulation of the cytokine GM-CSF induces spontaneous phagocyte invasion and immunopathology in the central nervous system. *Immunity* **46**, 245–260 (2017).
- Rapalino, O. et al. Implantation of stimulated homologous macrophages results in partial recovery of paraplegic rats. *Nat. Med.* **4**, 814–821 (1998).
- Weber, M. S. et al. Type II monocytes modulate T cell-mediated central nervous system autoimmune disease. *Nat. Med.* **13**, 935–943 (2007).
- Miron, V. E. et al. M2 microglia and macrophages drive oligodendrocyte differentiation during CNS remyelination. *Nat. Neurosci.* **16**, 1211–1218 (2013).
- Hu, X. et al. Microglial and macrophage polarization—new prospects for brain repair. *Nat. Rev. Neurol.* **11**, 56–64 (2015).
- Mills, E. L., Kelly, B. & O'Neill, L. A. J. Mitochondria are the powerhouses of immunity. *Nat. Immunol.* **18**, 488–498 (2017).
- Kroner, A. et al. TNF and increased intracellular iron alter macrophage polarization to a detrimental M1 phenotype in the injured spinal cord. *Neuron* **83**, 1098–1116 (2014).
- Shechter, R. et al. Recruitment of beneficial M2 macrophages to injured spinal cord is orchestrated by remote brain choroid plexus. *Immunity* **38**, 555–569 (2013).
- Galván-Peña, S. & O'Neill, L. A. Metabolic reprogramming in macrophage polarization. *Front. Immunol.* **5**, 420 (2014).
- Ransohoff, R. M. A polarizing question: do M1 and M2 microglia exist? *Nat. Neurosci.* **19**, 987–991 (2016).
- Béchade, C., Colasse, S., Diana, M. A., Rouault, M. & Bessis, A. NOS2 expression is restricted to neurons in the healthy brain but is triggered in microglia upon inflammation. *Glia* **62**, 956–963 (2014).
- Reese, T. A. et al. Chitin induces accumulation in tissue of innate immune cells associated with allergy. *Nature* **447**, 92–96 (2007).
- Yamasaki, R. et al. Differential roles of microglia and monocytes in the inflamed central nervous system. *J. Exp. Med.* **211**, 1533–1549 (2014).
- Vogl, T. et al. Autoinhibitory regulation of S100A8/S100A9 alarmin activity locally restricts sterile inflammation. *J. Clin. Invest.* **128**, 1852–1866 (2018). 10/1172/JCI89867.
- Rhee, S. G. & Kil, I. S. Multiple functions and regulation of mammalian peroxiredoxins. *Annu. Rev. Biochem.* **86**, 749–775 (2017).
- Rantakari, P. et al. Stabilin-1 expression defines a subset of macrophages that mediate tissue homeostasis and prevent fibrosis in chronic liver injury. *Proc. Natl. Acad. Sci. USA* **113**, 9298–9303 (2016).
- Xu, J., Xiao, N. & Xia, J. Thrombospondin 1 accelerates synaptogenesis in hippocampal neurons through neuroligin 1. *Nat. Neurosci.* **13**, 22–24 (2010).
- Goldmann, T. et al. Origin, fate and dynamics of macrophages at central nervous system interfaces. *Nat. Immunol.* **17**, 797–805 (2016).
- Iqbal, A. J. et al. Human CD68 promoter GFP transgenic mice allow analysis of monocyte to macrophage differentiation in vivo. *Blood* **124**, e33–e44 (2014).
- Schläger, C. et al. Effector T-cell trafficking between the leptomeninges and the cerebrospinal fluid. *Nature* **530**, 349–353 (2016).
- Kolodziejewski, P. J., Koo, J. S. & Eissa, N. T. Regulation of inducible nitric oxide synthase by rapid cellular turnover and cotranslational down-regulation by dimerization inhibitors. *Proc. Natl. Acad. Sci. USA* **101**, 18141–18146 (2004).
- Cantuti-Castelvetri, L. et al. Defective cholesterol clearance limits remyelination in the aged central nervous system. *Science* **359**, 684–688 (2018).
- Derecki, N. C. et al. Regulation of learning and memory by meningeal immunity: a key role for IL-4. *J. Exp. Med.* **207**, 1067–1080 (2010).
- Engelhardt, B., Vajkoczy, P. & Weller, R. O. The movers and shapers in immune privilege of the CNS. *Nat. Immunol.* **18**, 123–131 (2017).
- Louveau, A. et al. Understanding the functions and relationships of the glymphatic system and meningeal lymphatics. *J. Clin. Invest.* **127**, 3210–3219 (2017).
- Geissmann, F. et al. Development of monocytes, macrophages, and dendritic cells. *Science* **327**, 656–661 (2010).
- Van den Bossche, J. et al. Mitochondrial dysfunction prevents repolarization of inflammatory macrophages. *Cell Rep* **17**, 684–696 (2016).
- Mills, E. L. et al. Succinate dehydrogenase supports metabolic repurposing of mitochondria to drive inflammatory macrophages. *Cell* **167**, 457–470.e13 (2016).
- Murray, P. J. et al. Macrophage activation and polarization: nomenclature and experimental guidelines. *Immunity* **41**, 14–20 (2014).
- Ponomarev, E. D., Maresz, K., Tan, Y. & Dittel, B. N. CNS-derived interleukin-4 is essential for the regulation of autoimmune inflammation and induces a state of alternative activation in microglial cells. *J. Neurosci.* **27**, 10714–10721 (2007).
- Murray, P. J. & Wynn, T. A. Protective and pathogenic functions of macrophage subsets. *Nat. Rev. Immunol.* **11**, 723–737 (2011).
- Liddiard, K. & Taylor, P. R. Understanding local macrophage phenotypes in disease: shape-shifting macrophages. *Nat. Med.* **21**, 119–120 (2015).
- Kigerl, K. A. et al. Identification of two distinct macrophage subsets with divergent effects causing either neurotoxicity or regeneration in the injured mouse spinal cord. *J. Neurosci.* **29**, 13435–13444 (2009).
- Mikita, J. et al. Altered M1/M2 activation patterns of monocytes in severe relapsing experimental rat model of multiple sclerosis. Amelioration of clinical status by M2 activated monocyte administration. *Mult. Scler.* **17**, 2–15 (2011).
- Giles, D. A. et al. Myeloid cell plasticity in the evolution of central nervous system autoimmunity. *Ann. Neurol.* **83**, 131–141 (2018).
- Auffray, C., Sieweke, M. H. & Geissmann, F. Blood monocytes: development, heterogeneity, and relationship with dendritic cells. *Annu. Rev. Immunol.* **27**, 669–692 (2009).
- Nahrendorf, M. et al. The healing myocardium sequentially mobilizes two monocyte subsets with divergent and complementary functions. *J. Exp. Med.* **204**, 3037–3047 (2007).
- Arnold, L. et al. Inflammatory monocytes recruited after skeletal muscle injury switch into antiinflammatory macrophages to support myogenesis. *J. Exp. Med.* **204**, 1057–1069 (2007).
- Misharin, A. V. et al. Nonclassical Ly6C(–) monocytes drive the development of inflammatory arthritis in mice. *Cell Rep* **9**, 591–604 (2014).
- Rothhammer, V. et al. Type I interferons and microbial metabolites of tryptophan modulate astrocyte activity and central nervous system

inflammation via the aryl hydrocarbon receptor. *Nat. Med.* **22**, 586–597 (2016).

50. Liddel, S. A. et al. Neurotoxic reactive astrocytes are induced by activated microglia. *Nature* **541**, 481–487 (2017).

### Acknowledgements

We thank A. Schmalz, L. Schödel, and B. Fiedler for excellent technical assistance; D. Matzek and B. Stahr for animal husbandry; D. Kofink for help with statistical analysis; and E. Beltran for help with the flow cytometry analysis. We thank R. Hohlfeld and H. Wekerle for critical reading of the manuscript. Work in M.K.'s laboratory is financed through grants from the Deutsche Forschungsgemeinschaft (DFG; Transregio 128, Project B10), the European Research Council under the European Union's Seventh Framework Program (FP/2007-2013; ERC Grant Agreement n. 310932), the German Multiple Sclerosis Society (DMSG), the "Verein Therapieforschung für MS-Kranke e.V.", and the Munich Center for Systems Neurology (SyNergy; EXC 1010). M.P. is supported by the Sobek-Stiftung, the DFG (SFB 992, SFB1140, SFB/TRR167, Reinhart-Koselleck-Grant), and the Sonderlinie Hochschulmedizin Baden Württemberg, project "neuroinflammation in neurodegeneration". M.K. and M.P. are further supported by the German Federal Ministry of Research and Education (BMBF; Competence Network Multiple Sclerosis), and M.K. and M.S. are supported by a common grant from the DFG (Transregio 128, Project B13). G.L. was supported by fellowships from EMBO and Swiss National Science Foundation.

### Author contributions

G.L., D.T., M.P., and M.K. conceived and designed the experiments. G.L. and D.T. performed FACS experiments, imaging experiments, and image analysis. G.L., D.T., A.K., L.C.-C., M.S., and A.D. established and performed in situ and in vitro analyses of phagocyte polarization. G.L., M.J.C.J., O.S., and M.P. performed and analyzed RNAseq experiments; K.P. and F.M. performed and analyzed proteomics experiments; and A.B. generated and characterized the iNOS-tdTomato-Cre mouse line. G.L., D.T., and M.K. wrote the manuscript.

### Competing interests

The authors declare no competing interests.

### Additional information

**Supplementary information** is available for this paper at <https://doi.org/10.1038/s41593-018-0212-3>.

**Reprints and permissions information** is available at [www.nature.com/reprints](http://www.nature.com/reprints).

**Correspondence and requests for materials** should be addressed to M.K.

**Publisher's note:** Springer Nature remains neutral with regard to jurisdictional claims in published maps and institutional affiliations.

## Methods

**Mice.** C57BL/6 mice were obtained from Janvier Labs (Saint Berthevin Cedex, France). In addition we used the following genetically modified mouse lines: iNOS-tdTomato-Cre mice<sup>20</sup>, Arginase-YFP mice<sup>21</sup> (C.129S4/(B6)-Arg1<sup>tm1.1ky/j</sup>), CD68-GFP mice<sup>28</sup> (C57BL/6-Tg(CD68-EGFP)1Drg/j), Rosa26-Stp-fl-YFP mice (B6.Cg-Gt(Rosa)26Sor<tm3(CAG-EYFP)Hze>/J), CCR2<sup>RFP/+</sup> mice (B6.129(Cg)-Ccr2<sup>tm2.116/j</sup>) and CX3CR1<sup>GFP/+</sup> mice (B6.129P-Cx3cr1<sup>tm1.1at/j</sup>). All genetically modified mouse lines except for the iNOS-tdTomato-Cre were obtained from The Jackson Laboratory (Bar Harbor, Maine). The presence of respective transgenes was confirmed by PCR analysis on DNA from tail biopsies by use of the following primer pairs: for iNOS-tdTomato-Cre, *Cre* forward, GCA TTA CCG GTC GAT GCA ACG AGT GAT GAG; *Cre* reverse, GAG TGA ACG AAC CTG GTC GAA ATC AGT CGC; for Arginase-YFP and Rosa26-stop-fl-YFP, *YFP* forward, ATC TTC TTC AAG GAC GAC GGC AAC TAC AAG; *YFP* reverse, AGA GTG ATC CCG GCG GCG GTC ACG AAC TCC; for CD68-GFP, *GFP* forward, GCA CGA CTT CTT CAA GTC CGC CAT GCC; *GFP* reverse, GCG GAT CTT GAA GTT CAC CTT GAT GCC; for CX3CR1<sup>GFP/+</sup>, *GFP* forward GCA GCA CGA CTT CTT CAA GTC CGC CAT GCC; *GFP* reverse, GTG GCG GAT CTT GAA GTT GCG CTT GAT GCC; for CCR2<sup>RFP/+</sup>, *RFP* forward, TAA ACC TGG TCA CCA CAT GC; *RFP* wild-type reverse, GGA GTA GAG TGG AGG CAG GA; *RFP* mutant reverse, CTT GAT GAC GTC CTC GGA G. In all experiments, adult animals (minimum 6 weeks of age) from both sexes were used. All in vivo manipulations were performed following either KX or MMF-induced anesthesia. All animal experiments were performed in accordance with regulations of the relevant animal welfare acts and protocols approved by the respective regulatory bodies (Regierung von Oberbayern).

**EAE induction.** Active EAE was induced in adult mice by injecting 400 µg of purified recombinant MOG (N1-125) in complete Freund's adjuvant (containing 10 mg/mL *Mycobacterium tuberculosis* H37 Ra, Sigma-Aldrich). At days 0 and 2, 400 ng of pertussis toxin (Sigma-Aldrich) was administered intraperitoneally (i.p.). After immunization, mice were weighed daily and neurological deficits were evaluated according to the following EAE score: 0, no clinical signs; 0.5, partial tail weakness; 1, tail paralysis; 1.5, gait instability or impaired righting ability; 2, hind limb paresis; 2.5, hind limb paresis with dragging of one foot; 3, total hind limb paralysis; 3.5, hind limb paralysis and fore limb paresis; 4, hind limb and fore limb paralysis; 5, death. The 'weight loss' stage was defined as the first timepoint at which immunized mice lost weight; 'onset' as the first day of neurological symptoms; 'peak' as 2–3 d following clinical onset; 'remission' as 7 d following start of EAE.

**Bone marrow-derived macrophage culture.** For preparation of bone marrow suspension, the bones of the hind limbs and pelvis of Arginase-YFP, iNOS-tdTomato-Cre, iNOS-tdTomato-Cre × Arginase-YFP, and C57BL/6 control mice were flushed with ice-cold RPMI-1640 (Sigma-Aldrich) supplemented with 10% FCS (Sigma-Aldrich) and 100 U/mL penicillin/streptomycin. Suspension was filtered through 70-µm cell strainers (Falcon), and ACK buffer (Thermo Scientific) was added for 5 min on ice. Cells were resuspended in RPMI-1640 (Sigma-Aldrich) supplemented with 10% FCS (Sigma-Aldrich), 100 U/mL penicillin/streptomycin, and 5 ng/mL of macrophage colony stimulating factor (mCSF, R&D Systems) and transferred to eight-well Nunc Lab-Tek slides (Sigma-Aldrich) at a concentration of 2.5 million/mL. After 7 d of in vitro cultivation, the growth medium was replaced by either mCSF-supplemented phenol red-free RPMI-1640 (Sigma-Aldrich) medium (nonpolarized control), recombinant IL-4 (10 ng/mL) and IL-13 (10 ng/mL)-supplemented medium for anti-inflammatory polarization, or lipopolysaccharide (100 ng/mL) and IFNγ (10 ng/mL)-supplemented medium for proinflammatory polarization. Cells were either cultured for 48 h in the respective media and then fixed by incubation with 4% PFA for 10 min on ice (Supplementary Fig. 1) or cultured for 48 h followed by washing steps and 72 h incubation in either mCSF-supplemented RPMI-1640 (Sigma-Aldrich) medium (nonpolarized control), recombinant IL-4 (10 ng/mL) and IL-13 (10 ng/mL)-supplemented medium for anti-inflammatory polarization, or lipopolysaccharide (100 ng/mL) and IFNγ (10 ng/mL)-supplemented medium for proinflammatory polarization (Fig. 8). Sections were blocked with 10% goat serum in PBS with 0.5% Triton for 1 h at room temperature (20–25 °C) and stained with antibodies (in 1% goat serum and 0.5% Triton for 1 h) against the following antigens: iNOS (ABN26, Millipore), I-A/I-E (M5/114.15.2, BD Pharmingen), p22-phox (sc-20781, Santa Cruz), and tdTomato (16D7, Kerafast) for cells derived from iNOS-tdTomato-Cre and C57BL/6 control mice; or iNOS (ABN26, Millipore), YMI (01404, StemCell Technologies), CD206 (MR5D3, BioLegend), and GFP (ab13970, Abcam) for cells derived from Arginase-YFP and C57BL/6 control mice; or GFP (ab13970, Abcam) and tdTomato (16D7, Kerafast) for cells derived from iNOS-tdTomato-Cre × Arginase-YFP mice. Detection was accomplished using incubation with Alexa Fluor-coupled secondary antibodies (Life Technologies) in PBS supplemented with 1% goat serum and 0.5% Triton for 1 h at room temperature. A nuclear counterstaining using DAPI (Thermo Fisher) was performed for 10 min at room temperature. Sections were covered with Vectashield (Vector Laboratories) and coverslips fixed with clear nail polish. Samples were scanned on an upright FV1000 confocal microscopy system (Olympus) equipped with

20×/0.85 oil immersion objective, zoom 3.5×, and image size 1,024 × 1,024 pixels. Images were acquired using standard filter sets and processed with Fiji or Adobe Photoshop software.

The absolute values of antibody-specific fluorescent intensities were calculated after subtracting both background signal and appropriate isotype control-fluorescence. YFP and tdTomato-specific fluorescent intensities shown in Supplementary Fig. 1 were calculated after subtracting both background signal and staining intensity detected in control C57BL/6 mice. For image representation, pictures were processed with a Despeckle or Dust and Scratches filter using Photoshop software (Adobe).

**Injection of BMDMs in the spinal cord.** BMDM for spinal cord injection were prepared from bone marrow suspension of iNOS-tdTomato-Cre × CD68-GFP mice and polarized to a proinflammatory phenotype as described above. Cells were detached after 10-min Trypsin incubation, loaded into finely drawn glass micropipettes, and following a laminectomy, stereotactically injected in the spinal cord white matter of healthy mice or mice at clinical onset of EAE. Mice were perfused transcardially with PBS followed by 4% paraformaldehyde (PFA) at 24 or 72 h postinjection. The spinal cords were dissected, postfixed for 12 h with 4% PFA, cryoprotected in 30% sucrose (Sigma-Aldrich), embedded in Tissue-Tek (Sakura Finetek Europe B.V.), and frozen at –20 °C.

**Analysis of the effects of phagocytosis and glial cells on BMDMs.** For microglia isolation, mouse brains from postnatal day 8 mice were isolated and cut into small pieces. The brains were then reduced to a single cell suspension with the Neural Dissociation Kit (Miltenyi Biotec), according to the manufacturer's instructions. The cell suspension was passed through a 70-µm strainer and the cells were counted. The cells were then pelleted and resuspended in DMEM with magnetic beads against CD11b. After magnetic isolation, the cells were plated and expanded for 6 d in media containing MCSF (50 ng/mL). Astrocytes were prepared as previously described<sup>31</sup>. Briefly, P1 mouse brains were isolated and digested to a single-cell suspension with 0.05% trypsin. The cells were plated on a poly-D-lysine-coated flask and left to grow for 7 d. Microglia and oligodendrocytes were then removed by shaking the flask, leaving the astrocyte carpet intact.

Myelin was isolated as previously described<sup>31</sup>. Briefly, 8-week-old C57BL/6 mouse brains were homogenized by sonication in 10 mM HEPES, 5 mM EDTA, and 0.3 M sucrose. The homogenate was then layered on a sucrose gradient of 0.32 M and 0.85 M sucrose in 10 mM HEPES + 5 mM EDTA (pH 7.4) and centrifuged at 75,000 g for 30 min with a SW32 Ti rotor. The pellet (nonmyelin fraction) was resuspended in 10 mM HEPES buffer, while the first (crude) myelin fraction was isolated from the interface and subjected to three additional rounds of osmotic shock in ultrapure water and centrifugation at 75,000 g for 15 min. The pellet was then subjected to the same protocol to obtain a pure myelin fraction. The amount of isolated myelin was calculated by measuring the amount of protein with the Bradford assay (BioRad, 500-0006).

BMDMs were cultured in vitro and polarized to an M<sup>PO</sup> phenotype for 48 h as described above. Polarized BMDMs then were washed several times and co-cultured with 1 × 10<sup>6</sup> U/mL Fluoresbrite YG Microspheres 1.00 µm (Polysciences; 'beads'), 4 × 10<sup>6</sup> U/mL Zymosan A (*S. cerevisiae*) BioParticles (Thermo Fischer Scientific; 'TLR beads'), 40 mg/mL myelin and nonmyelin fraction of the CNS (prepared as described above), respectively, for 24 h. Microglia and astrocytes (1 × 10<sup>6</sup> U/mL, prepared as described above) were seeded on the upper compartment of an 0.4-µm pore-size (PET) cell-culture Transwell insert (Merck) and co-cultured with M<sup>PO</sup> phagocytes for 24 h. After treatment, total RNA was isolated from BMDMs using the RNeasy Mini Kit (Qiagen) according to the manufacturer's instructions. RNA concentration and purity were measured by Nanodrop. cDNA was synthesized using RevertAid H Minus First Strand cDNA synthesis kit (Thermo Fischer Scientific) with 400–500 ng total RNA and Oligo (dt) primers. Quantitative PCR (qPCR) was carried out on a BioRad CFX Connect Real-Time PCR system using specific primer pairs for iNOS (forward, 5'-CCG AAG CAA ACA TCA CAT TCA-3'; reverse, 5'-GGT CTA AAG GCT CCG GGC T-3') and for *Arg1* (forward, 5'-CTC CAA GCC AAA GTC CTT AGA G-3'; reverse, 5'-AGG AGC TGT CAT TAG GGA CAT C-3')<sup>31</sup> and with SsoAdvanced Universal SYBR Green Supermix (BioRad). BMDMs, microglia, and astrocytes were isolated from three C57BL/6 mice and all qPCR reactions were run in duplicate; the housekeeping gene *Gapdh* was used as an internal control to normalize the variability in expression level. Results were quantified using the  $\Delta\Delta C_t$  method. All fold changes are normalized to the control BMDMs cultured with medium only.

**Flow cytometry.** For analysis of cell populations in the CNS, mice were killed and their CNS was isolated and transferred to ice-cold PBS (Sigma-Aldrich). Tissue was cut in small pieces and digested in RPMI containing 2% FCS (Sigma-Aldrich), 25 mM HEPES (Sigma-Aldrich), 10 ng/mL DNase I (StemCell Technologies) and 0.8 mg/mL Collagenase D (Roche) for 30 min at 37 °C. Reaction was stopped by adding 1:100 dilution of an 0.5-M EDTA (Sigma-Aldrich) solution. Suspension was filtered through 70-µm cell strainers (Falcon) and resuspended in a 30% solution of Percoll (Sigma-Aldrich). After 30 min of gradient centrifugation at 12,000 g, the top (myelin) and lower (red cells) layers were removed and the remaining

solution was filtered through 70- $\mu\text{m}$  cell strainers (Falcon). For blood analysis, blood was collected from the heart or submandibular vein in heparin-coated tubes. Erythrocytes were removed by incubation with FACS Lysing solution (BD Biosciences) for 10 min on ice. For analysis of cell populations in lymph nodes, mice were killed, and the inguinal and axillary lymph nodes were isolated and mechanically dissociated in ice-cold PBS (Sigma-Aldrich) using glass slides. The suspension was filtered through 70- $\mu\text{m}$  cell strainers (Falcon).

Stainings were performed in ice-cold PBS after Fc-receptor blockade (CD16/32, 1  $\mu\text{L}$ /million cells, clone 2.4G2, BD Biosciences) using LIVE/DEAD staining (Invitrogen) and the following antibodies: CD45 (clone 30-F11, BioLegend), CD11b (clone M1/70, BD Biosciences), CD11c (clone N418, Abcam), F4/80 (clone BM8, eBiosciences), Ly6C (clone AL21, BD Biosciences), Ly6G (clone 1A8, Biolegend), CD40 (clone HM40-3, Biolegend), MHC-II (clone M5/114.15.2, BD Bioscience), CD80 (clone 16-10A1, Biolegend), and CD86 (clone GL-1, Biolegend). Samples were acquired on an LSR-Fortessa cytometer (BD Biosciences) and results analyzed by FlowJo software. For intracellular stainings, cells were incubated in complete RPMI supplemented with GolgiPlug (BD Biosciences) for 4 h at 37°C and permeabilized with a Cytotfix/Cytoperm kit (BD Biosciences) before staining with antibodies specific to LAP (TGF $\beta$ , clone TW7-16B4, Biolegend), TNF $\alpha$  (clone MP6-XT22, Biolegend), IL1Ra (clone EPR6483, Abcam), and IL1 $\beta$  (clone NJTEN3, eBioscience).

The average percentage of polarized cells isolated from the CNS of control C57BL/6 mice was  $0.62 \pm 0.03$  for M<sup>iNOS</sup>,  $0.06 \pm 0.03$  for M<sup>iNOS/Arginase</sup>, and  $0.26 \pm 0.1$  for M<sup>Arginase</sup> cells in the CD45<sup>high</sup>CD11b<sup>low</sup> population;  $1.55 \pm 0.3$  for M<sup>iNOS</sup>,  $0.29 \pm 0.1$  for M<sup>iNOS/Arginase</sup> and  $0.7 \pm 0.2$  for M<sup>Arginase</sup> cells in the CD45<sup>int</sup>CD11b<sup>int</sup> population; and  $0.56 \pm 0.25$  for M<sup>iNOS</sup>,  $0.16 \pm 0.06$  for M<sup>iNOS/Arginase</sup> and  $0.25 \pm 0.07$  for M<sup>Arginase</sup> cells in the CD45<sup>high</sup>CD11b<sup>high</sup> population.

Within the CD45<sup>high</sup>CD11b<sup>high</sup> population isolated from iNOS-tdTomato-Cre $\times$ Arginase-YFP mice, a small percentage of Ly6G<sup>+</sup> granulocytes also showed expression of the reporter genes. The relative percentage of polarized granulocytes compared to Ly6G<sup>-</sup> cells in the same CD45<sup>high</sup>CD11b<sup>high</sup> gate was  $1.4 \pm 0.28$  for M<sup>iNOS</sup>,  $0.6 \pm 0.1$  for M<sup>iNOS/Arginase</sup>, and  $0.4 \pm 0.1$  for M<sup>Arginase</sup> cells.

**RNA-sequencing analysis.** Cells were isolated from the CNS of iNOS-tdTomato-Cre $\times$ Arginase-YFP mice at clinical onset or at peak of EAE as described above, stained with LIVE/DEAD staining (eBioscience), CD45 (clone 30-F11, eBioscience), CD11b (clone M1/70, eBioscience), and CD64 (clone X54-5/7.1, BD), and sorted through a FACS Aria III (Becton Dickinson) based on relative expression of the reporter proteins YFP and tdTomato and expression of CD11b and CD45. Blood monocytes were isolated from the blood of iNOS-tdTomato-Cre $\times$ Arginase-YFP mice at clinical onset of disease based on CD45, CD11b, and CD115 expression. Total RNA was extracted from cells stabilized in RNAprotect buffer according to the protocol of the RNeasy Plus Micro Kit (QIAGEN). In brief, cells were stored and shipped in RNAprotect buffer at 2–8°C. After pelleting, the RNAprotect buffer was replaced by RLT Plus and the samples were homogenized by vortexing for 30 s. Genomic DNA contamination was removed using gDNA Eliminator spin columns. Next, ethanol was added, and the samples were applied to RNeasy MinElute spin columns followed by several washing steps. Total RNA was eluted in 12  $\mu\text{L}$  of nuclease-free water. RNA purity and integrity was assessed on an Agilent 2100 Bioanalyzer with an RNA 6000 Pico LabChip reagent set (Agilent). The SMARTer Ultra Low Input RNA Kit for Sequencing v4 (Clontech Laboratories, Inc.) was used to generate first strand cDNA from 100 to 500 pg total RNA. Double-stranded cDNA was amplified by LD PCR (13 or 14 cycles) and purified via magnetic bead cleanup. Library preparation was carried out as described in the Illumina Nextera XT Sample Preparation Guide (Illumina). Using the Nextera XT transposome, 150 pg of input cDNA were tagged and fragmented. The products were purified and amplified via a limited-cycle PCR program to generate multiplexed sequencing libraries. For the PCR step, 1:5 dilutions of index 1 (i7) and index 2 (i5) primers were used. The libraries were quantified using the KAPA SYBR FAST ABI Prism Library Quantification Kit (Kapa Biosystems, Inc.). Equimolar amounts of each library were pooled and used for cluster generation on the cBot with the Illumina TruSeq SR Cluster Kit v3. The sequencing run was performed on a HiSeq 1000 instrument using the indexed, 50-cycle single-read (SR) protocol and TruSeq SBS v3 reagents according to the Illumina HiSeq 1000 System user guide. Image analysis and base calling resulted in .bcl files, which were converted into .fastq files with the CASAVA1.8.2 software. RNA isolation, library preparation, and RNAseq were performed at the Genomics Core Facility, KFB - Center of Excellence for Fluorescent Bioanalytics (University of Regensburg, Regensburg, Germany).

Fastq files were quality controlled using FastQC<sup>52</sup>, and reads were mapped to the GRCh38 mouse genome using the Star aligner<sup>53</sup>. Read counts were obtained by the featureCounts package<sup>54</sup>, and differential gene expression analysis was performed using the limma/voom pipeline in R<sup>55,56</sup>. Highly and statistically significant differentially expressed genes were defined using a cutoff of log<sub>2</sub>(fold-change) and adjusted  $P < 0.05$  following the suggestions by the SEQ consortium<sup>57</sup>. PCA analysis was performed using the pcomp package within the R stats library<sup>56</sup>. Venn diagrams were created using the R library VennDiagram<sup>58</sup>. The full dataset has been deposited online (GEO submission number GSE107792).

**Sample preparation and mass spectrometry (LC-MS/MS).** For mass spectrometry analysis, M<sup>iNOS</sup>, M<sup>iNOS/Arginase</sup>, and M<sup>Arginase</sup> cells, as well as unpolarized

phagocytes, were isolated from the CNS of iNOS-tdTomato-Cre $\times$ Arginase-YFP mice at peak of EAE as described above, stained with LIVE/DEAD staining (eBioscience), CD45 (clone 30-F11, eBioscience), CD11b (clone M1/70, eBioscience), and Ly6G (clone 1A8, Biolegend), and sorted through a FACS Aria III (Becton Dickinson) based on relative expression of the reporter proteins YFP and tdTomato and expression of CD11b and CD45. Ly6G<sup>+</sup> cells were excluded from the analysis. The cells (100,000 to 500,000 cells per sample) were pelleted, snap-frozen in liquid nitrogen and stored at –80°C until further processing. Frozen cells were resuspended in 50  $\mu\text{L}$  of digestion buffer containing 1% SDC, 10 mM TCEP, 55 mM CAA, 25 mM Tris, pH 8, and boiled for 10 min to denature proteins. After sonication using a Bioruptor, proteins were digested with 1  $\mu\text{g}$  Lys-C and Trypsin with shaking, overnight at 37°C. Peptides were desalted and purified using two discs of SDB-RPS material and resuspended in 2% acetonitrile/0.1% TFA for LC-MS.

Reverse phase chromatographic separation of peptides was performed by loading approximately 200–500 ng of peptides on a 50-cm HPLC-column (75- $\mu\text{m}$  inner diameter; in-house packed using ReproSil-Pur C18-AQ 1.9- $\mu\text{m}$  silica beads; Dr. Maisch GmbH, Germany) coupled to an EASYnLC 1200 ultra-high-pressure system (Thermo Fisher Scientific). Peptides were separated with a buffer system consisting of 0.1% formic acid (buffer A) and 80% acetonitrile in 0.1% formic acid (buffer B) using a linear gradient from 5 to 30% B in 155 min. The column temperature was set to 60°C. The LC was coupled to a quadrupole Orbitrap mass spectrometer (Q Exactive HFX, Thermo Fisher Scientific, Rockford, IL, USA) via a nano-electrospray ion source. The mass spectrometer was operated in data-dependent acquisition mode, collecting MS1 spectra (60,000 resolution, 300–1,650  $m/z$  range) with an automatic gain control (AGC) target of  $3 \times 10^6$  and a maximum ion injection time of 20 ms. The 15 most-intense ions from the MS1 scan were isolated with an isolation width of 1.4  $m/z$ . Following higher-energy collisional dissociation (HCD) with a normalized collision energy (NCE) of 27%, MS2 spectra were collected (15,000 resolution) with an AGC target of  $5 \times 10^4$  and a maximum ion injection time of 28 ms. Dynamic precursor exclusion was enabled with a duration of 30 s.

**MS data processing and analysis.** Mass spectra were searched against the 2016 Uniprot mouse databases using MaxQuant<sup>59</sup> version 1.5.5.2 with a 1% FDR at the peptide and protein level. Peptides required a minimum length of seven amino acids with carbamidomethylation as a fixed modification and with N-terminal acetylation and methionine oxidations as variable modifications. Enzyme specificity was set C-terminal to arginine and lysine using trypsin as protease, and a maximum of two missed cleavages were allowed in the database search. The maximum mass tolerances for precursor and fragment ions were 4.5 ppm and 20 ppm, respectively. ‘Match between runs’ was enabled to transfer peptide identifications between individual measurements with an 0.7-min window after retention time alignment. Label-free quantification was performed with the MaxLFQ algorithm<sup>60</sup> using a minimum ratio count of 2. Protein identifications were filtered by removing matches to the reverse database, matches only identified by site, and common contaminants. Data filtering and statistical analysis were performed with Perseus v1.5.5.5<sup>61</sup>, GraphPad Prism v7.03, Microsoft Excel, and R Studio v3.4.0. Data were further filtered such that only proteins with identifications in all replicates of one cell type were retained. Missing values were imputed from a normal distribution of intensity values at the detection limit of the mass spectrometer. Statistical analysis was performed as indicated in the figure legends, with a constant permutation-based FDR correction at 5%. Data are available via ProteomeXchange with identifier PXD010245.

**Immunohistochemistry and in situ confocal microscopy.** Mice were killed with isoflurane and perfused transcardially with PBS followed by 4% paraformaldehyde (PFA). The spinal cords were dissected, postfixed for 12 h with 4% PFA, cryoprotected in 30% sucrose (Sigma-Aldrich), embedded in Tissue-Tek (Sakura Finetek Europe B.V.), and frozen at –20°C. Frozen tissue was cut sagittally in 30- to 50- $\mu\text{m}$ -thick sections using a cryostat (Leica). Antigen retrieval was performed in a sodium citrate buffer (pH 8.5) for 30 min at 85°C. Sections were blocked with PBS supplemented with 10% goat serum and 0.1% Triton for 30 min and stained with antibodies in PBS supplemented with 2% goat serum and 0.1% Triton at 4°C overnight. Stainings were performed against the following antigens: iNOS (ABN26, Millipore), arginase-1 (sc-20150, Santa Cruz), tdTomato (16D7, Kerafast; used for amplification of tdTomato and RFP in sections processed for immunohistochemistry), GFP (ab13970, Abcam; used for amplification of YFP and GFP in sections processed for immunohistochemistry), Iba-1 (019-19741, Wako), Olig2 (AB9610, Chemicon International), GFAP (G9269, Sigma-Aldrich), and CD3 (CD3-12, Serotec). Detection was accomplished by incubation with Alexa Fluor-coupled secondary antibodies (Life Technologies/Abcam) diluted in PBS supplemented with 2% goat serum and 0.1% Triton, for 3 h at room temperature. For the Iba-1 immunostaining depicted in Supplementary Fig. 2b, sections were blocked with 10% goat serum and 0.5% Triton in PBS for 1 h and incubated with an Iba-1-specific antibody (019-19741, Wako) diluted in PBS supplemented with 1% goat serum and 0.5% Triton at 4°C, overnight. Detection was accomplished by incubation with an Alexa Fluor 647-coupled secondary antibody (Life Technologies) for 3 h at room temperature in PBS supplemented with 1% goat

serum and 0.5% Triton. For laminin immunostaining, sections were blocked with 10% goat serum and 0.4% Triton in 0.1 M PB solution for 1 h and incubated with a laminin-specific antibody (ab11575, Abcam) diluted in 0.1 M PB supplemented with 5% goat serum and 0.4% Triton at 4°C, overnight. Detection was accomplished by incubation with an Alexa Fluor 647-coupled secondary antibody (Life Technologies) for 2 h at room temperature in 0.1 M PB supplemented with 5% goat serum 0.4% Triton. Cell nuclei were staining using DAPI (Thermo Fisher) for 10 min at room temperature. Sections were covered with Vectashield (Vector Laboratories), and coverslips were fixed with clear nail polish. Samples were scanned on an upright FV1000 confocal microscope system (Olympus) equipped with 10×/0.4 air, 20×/0.85 oil-immersion, and 60×/1.35 oil-immersion objectives. Images were acquired using standard filter sets and processed with Fiji software. For image presentation, pictures were processed using Photoshop software (Adobe) with a Despeckle or a Dust and scratches filter.

**Quantitative analysis of in situ images.** Co-localization of tdTomato and YFP with the cell-type markers Iba-1, Olig2, GFAP, and CD3 was visually assessed in sections derived from single-transgenic iNOS-tdTomato-Cre and Arginase-YFP mice perfused at peak of EAE.

The co-localization of tdTomato and YFP reporter proteins with iNOS- and arginase-1-immunoreactivity was assessed in single-transgenic iNOS-tdTomato-Cre (at weight loss) and Arginase-YFP mice (at remission) as follows. To quantify fluorescence intensities in individual cells, these were first outlined using Fiji software and saved as regions of interest (ROI). The fluorescence intensities in the respective channels were then measured for these ROI. Cells with background-corrected tdTomato and YFP intensities higher than the signal detected in control C57BL/6 sections (average fluorescent intensity + 3 s.d.) were included in the analysis. In these cells, background-corrected iNOS- and arginase-1-specific signals were measured and considered positive if they were higher than the signal detected in isotype control-stained sections from the same mice (average fluorescent intensity + 3 s.d.).

To determine the proportion of all phagocytes that were polarized, we counterstained sections from iNOS-tdTomato-Cre × Arginase-YFP for the phagocyte marker Iba-1. Iba-1<sup>+</sup> cells in a given EAE lesion were visually identified, and tdTomato and YFP intensities in these cells were measured as described above. Cells were considered to be nonpolarized if both tdTomato and YFP signal intensities were below the respective signals (average + 3 s.d.) detected in Arginase-YFP (for tdTomato) and iNOS-tdTomato-Cre (for YFP) mice at the same stage of EAE ( $n = 5$  or 6 iNOS-tdTomato × Arginase-YFP mice and  $n = 3$  for single-transgenics per timepoint). Proportions of nonpolarized cells over the course of EAE: at weight loss  $32.8 \pm 3.8\%$  (average  $\pm$  s.e.m.), cells analyzed = 1,425; at onset:  $22.3 \pm 1.3\%$  (average  $\pm$  s.e.m.), cells analyzed = 1,690; at EAE peak:  $9.1 \pm 1.2\%$  (average  $\pm$  s.e.m.), cells analyzed = 1,913; at remission:  $24.0 \pm 9.8\%$  (average  $\pm$  s.e.m.), cells analyzed = 1,926.

To analyze the proportions of  $M^{\text{iNOS}}$ ,  $M^{\text{iNOS/Arginase}}$ , and  $M^{\text{Arginase}}$  cells over the course of EAE, background-corrected tdTomato and YFP signal intensities were measured in individual cells (outlined as described above) located in sections from iNOS-tdTomato-Cre × Arginase-YFP mice. tdTomato and YFP signals were considered positive if they were higher than those (average fluorescent intensity + 3 s.d.) detected in sections from Arginase-YFP (for tdTomato) and iNOS-tdTomato-Cre (for YFP) single-transgenic mice at the same stage of EAE ( $n = 5$  mice per group). To assess the dominant polarization of phagocytes, we determined the ratio of YFP/tdTomato intensities. When this ratio was  $> 5$ , cells were classified as  $M^{\text{Arginase}}$ ; when the ratio was  $< 0.2$ , cells were classified as  $M^{\text{iNOS}}$ ; and cells with ratios in between these values were classified as  $M^{\text{iNOS/Arginase}}$ . For this analysis, we quantified 724 cells from 6 mice at weight loss, 1,571 cells from 10 mice at onset, 1,976 cells from 8 mice at peak of disease, and 797 cells from 5 mice at remission.

To analyze the spatial distribution of polarized cells in EAE lesions at disease onset, cell-specific YFP and tdTomato intensities in iNOS-tdTomato-Cre × Arginase-YFP mice were calculated as described above. A square grid with  $400 \mu\text{m}^2$  area per section was overlaid on a given EAE lesion using Fiji software.  $M^{\text{iNOS}}$ ,  $M^{\text{iNOS/Arginase}}$ , and  $M^{\text{Arginase}}$  cell were classified as described above, and their densities were quantified per square. Individual squares were joined together in composite structures allowing analysis of horizontal bands starting from the pia surface, concentric squares starting from the lesion core, or bands parallel to and starting from the main vessel within the lesion area.

To analyze the proportion of resident and invading phagocytes expressing iNOS or Arginase, we killed CCR2<sup>REPL/+</sup> × CX3CR1<sup>GFP/+</sup> mice at the peak of EAE. GFP and RFP reporter intensities and arginase-1-specific antibody signals were first background-subtracted. GFP and RFP intensities were considered positive if they were higher than the respective signal (average + 3 s.d.) detected in C57BL/6 control mice at the peak of EAE. iNOS and arginase-1 immunostainings were considered positive if their fluorescence intensities were higher than the signal detected in isotype-control stainings of sections from the same mice (average + 3 s.d.;  $n = 4$  mice, 448 cells analyzed for iNOS and 516 cells analyzed for arginase-1).

To monitor the polarization of phagocytes after transfer to the spinal cord, spinal cord sections of mice injected with BMDMs isolated from iNOS-tdTomato-

Cre × CD68-GFP mice and polarized to a proinflammatory phenotype in vitro (as described above) were counterstained for arginase-1. GFP<sup>+</sup> cells were visually identified and tdTomato and arginase intensities in these cells were measured as described above. Arginase-1 immunostaining was considered positive if the fluorescence intensity was higher than the signal detected in isotype-control staining (average + 3 s.d.). tdTomato labeling was considered positive if the fluorescence intensity was higher than the average + 3 s.d. of the tissue background on the same sections ( $n = 5$  mice each for the injections in healthy mice killed after 24 and 72 h and  $n = 4$  mice for the injection in EAE mice).

Fate-tracking of arginase-1<sup>+</sup> phagocytes was performed in iNOS-tdTomato-Cre × Rosa26-Stp-fl-YFP mice perfused at peak of EAE as follows: tdTomato and YFP reporter intensities and arginase-1-specific antibody signals were first background-subtracted. tdTomato and YFP intensities were considered positive if they were higher than the respective signal (average + 3 s.d.) detected in Rosa26-Stp-fl-YFP control mice at peak. Arginase-1 immunostaining was considered positive if its fluorescence intensity was higher than the signal detected in isotype-control stainings of sections from the same mice (average + 3 s.d.). Total number of cells analyzed = 996,  $n = 4$  mice. The efficiency of Cre-mediated YFP expression in iNOS-tdTomato-Cre × Rosa26-Stp-fl-YFP mice was assessed by analyzing the presence of YFP in tdTomato<sup>+</sup> phagocytes.

**In vivo imaging and image processing.** Anesthetized mice were placed on a heating pad for 15 min. Tracheotomy and intubation were performed to minimize breathing artifacts, and the dorsal spinal cord was surgically exposed, superfused with artificial cerebrospinal fluid, and clamped as previously described<sup>62</sup>. Imaging was performed with an Olympus FV1200 MPE microscope equipped with a 25×/1.25 water immersion objective (Olympus), using 488-nm and 568-nm single-photon excitation, zoom 1–1.4×, step size 1.9–2.2  $\mu\text{m}$ , and image sizes of  $800 \times 800$  to  $1,024 \times 1,024$  pixels. To image large overview sections of spinal cords of iNOS-tdTomato-Cre × Arginase-YFP mice, vasculature was first revealed by i.p. injection of 200  $\mu\text{g}$  of Dextran-AF647 (Life Technologies). Image assembly was manually performed using Illustrator (Adobe). For image representation, pictures have been gamma-adjusted and processed with a Dust and scratches filter using Photoshop (Adobe). Supplementary Videos were assembled using Windows Maker (Windows).

**Quantitative analysis of in vivo images.** The different phagocyte polarization phenotypes in iNOS-tdTomato-Cre × Arginase-YFP mice were visually assessed based on fluorescent signals in the 488-nm and 568-nm channels. All cells expressing detectable amounts of YFP and tdTomato were categorized as  $M^{\text{iNOS/Arginase}}$ .

To quantify the polarized cells in the different CNS microenvironments of iNOS-tdTomato-Cre × Arginase-YFP mice, spinal EAE lesions were first identified based on the focal accumulation of polarized phagocytes in the meninges and upper layers of the spinal cord, and image stacks were acquired starting from the dura surface. Upper meninges were surgically removed as previously described<sup>63</sup>, and the lesion volume was re-acquired. Cells located in the upper meninges were identified as cells in the upper part of the image stack that were present before and absent after dura removal. Cells at the pia–parenchyma interface or in the parenchymal compartment were assessed following dura mater removal and distinguished based on their relative depth from the upper pia surface. More specifically, the top two cell layers from the pia layer (i.e., up to  $\sim 10 \mu\text{m}$  from tissue surface) were considered to be at the pia–parenchyma interface, while all polarized cells lying below the third cellular layer from the tissue surface were considered to be part of the parenchymal compartment. Analyzed number of lesions per animal: 2–4 lesions at weight loss, 1–3 lesions at onset, 2–3 lesions at peak and 2–3 lesions at remission.

For time-lapse imaging of iNOS-tdTomato-Cre × Arginase-YFP mice, spinal cord lesions were followed at 2-h intervals for a total of 6 h. Individual cells could be followed over time based on their location in the stack, their morphology, and the polarization pattern of neighboring cells. The in vivo phenotype of phagocytes was determined at all timepoints, as described above. To confirm the visual assessment of phenotype switching, we quantified YFP fluorescence signal (after background-subtraction) at 0 and 6 h in  $M^{\text{iNOS}}$  changing cells compared to  $M^{\text{iNOS}}$  cells that did not change their phenotype over time and that were lying at a comparable tissue depth. The YFP fluorescence fold-increase (average  $\pm$  s.d.) was  $4.01 \pm 0.38$  in changing cells at weight loss ( $1.65 \pm 0.19$  in unchanging cells),  $4.13 \pm 1.18$  in changing cells at onset ( $1.97 \pm 0.41$  in unchanging cells),  $7.64 \pm 2.01$  in changing cells at peak ( $2.57 \pm 0.64$  in unchanging cells), and  $3.12 \pm 0.3$  in changing cells at remission ( $0.83 \pm 0.16$  in unchanging cells). Localization (upper meninges, pia–parenchyma, or parenchyma) of polarized cells switching their phenotype was inferred based on the position of the respective cells in the stack and in relation to dura and pia mater reflectance.

For in vivo bleaching experiments in iNOS-tdTomato-Cre × Arginase-YFP mice, spinal lesions were first acquired at a low magnification (1.3×). Fluorescence bleaching was obtained by exposing the center of the lesion area (higher magnification, 4.3×, Kalman filter = 2) to 80% (488 nm) and 50% (568 nm) laser power. Starting tdTomato and YFP fluorescent intensity were bleached by the following percentages:  $78.4 \pm 1.8$  of tdTomato and  $36.3 \pm 1.5$  of YFP intensity

at weight loss,  $82.0 \pm 1.1$  of tdTomato and  $48.4 \pm 3.1$  of YFP intensity at onset,  $87.4 \pm 1.8$  of tdTomato and  $56.7 \pm 3.9$  of YFP intensity at peak of EAE, and  $77.1 \pm 1.6$  of tdTomato and  $45.4 \pm 2.5$  of YFP intensity at remission. The entire lesion area (magnification 1.3 $\times$ ) was re-acquired immediately (bleached image) and after 5 h. tdTomato and YFP fluorescence intensity in polarized cells was background-subtracted and quantified before bleaching, after bleaching, and after 5 h, both in the bleached area and in the surrounding nonaffected tissue. Cellular iNOS/arginase-1 promoters were considered active if the fluorescence of tdTomato and YFP (respectively) were increased by 30% or more compared to the average fluorescent change in unbleached cells over the same time-frame at 5 h compared to the immediate postbleaching values.

For time-lapse imaging of iNOS-tdTomato-Cre  $\times$  CD68-GFP mice, the vasculature was revealed as described above, and spinal cord lesions imaged at 3-h intervals for a total of 6 h. The proportion of GFP<sup>+</sup> phagocytes expressing tdTomato was visually assessed at the initial imaging timepoint. The localization of cells in the upper meninges at the pia–parenchyma border or within the parenchyma was visually inferred based on the relative position of the cell in the stack and in relation to the reflective signals originating from dura and pia mater as described and validated above. Cells within the lumen of the blood vessel, revealed by fluorescent labeling with Dextran-AF647, were considered to be vascular, while cells in contact with (but outside of) the vessel were considered to be perivascular. In situ validation in fixed tissue sections stained with an anti-Laminin antibody confirmed that in all cases investigated, such cells were indeed localized in the perivascular space as outlined by Laminin labeling ( $n=79$  cells, 3 mice). Number of cells analyzed at the pia–parenchyma interface = 4,355; in upper meninges = 2,727; in vasculature = 142; in perivascular space = 268, and in parenchyma = 1,778;  $n=7$  mice. To detect the initial polarization of GFP<sup>+</sup> cells, the tdTomato signal was visually assessed at the 3-h and 6-h timepoints in GFP<sup>+</sup> cells that lacked tdTomato fluorescence at 0 h. Number of cells analyzed in perivascular space = 51, in parenchyma = 197, in pia–parenchyma = 301, in upper meninges = 214,  $n=7$  mice.

**Randomization, exclusion, and blinding.** Randomization was not possible due to the experimental design (i.e., tdTomato and YFP reporters guided cell selection in all experiments). However, all analyses were performed using images displayed in grayscale to avoid color-driven analysis bias. No data were excluded from the study. Data collection and analysis were not performed blind due to the conditions of the experiments.

**Statistical analysis.** No statistical methods were used to predetermine sample sizes, but our sample sizes are similar to those reported in previous publications<sup>27,29</sup>. Datasets were tested for normality using Kolmogorov–Smirnov tests. We used  $t$  tests for two-sample comparisons and one-way or two-way ANOVA followed by Bonferroni's multiple-comparison tests for more than two samples, if the data were normally distributed; Mann–Whitney tests were performed for two-sample comparisons or Kruskal–Wallis tests with Dunn's post hoc comparisons for more than two samples, if the data were not normally distributed. If the sample size was too small to test for normality we assumed a normal distribution. Statistical analyses were performed with GraphPad Prism 7 software.

**Reporting Summary.** Further information on experimental design is available in the Nature Research Reporting Summary linked to this article.

**Code availability.** No custom code was used in this study. We used the following software for our analysis: limma/voom: <http://bioconductor.org/packages/release/bioc/html/limma.html>; featureCounts: <http://bioinf.wehi.edu.au/featureCounts/>; STAR: <https://github.com/alexdobin/STAR>.

**Accession codes and data availability.** The RNA-seq data have been deposited in GEO under accession number [GSE107792](https://www.ncbi.nlm.nih.gov/geo/query/acc.cgi?acc=GSE107792). The mass spectrometry proteomics data have been deposited with the ProteomeXchange Consortium via the PRIDE partner repository with identifier PXD010245. The overall data that support the findings of this study are available from the corresponding author upon reasonable request.

## References

- Lu, G. et al. Myeloid cell-derived inducible nitric oxide synthase suppresses M1 macrophage polarization. *Nat. Commun.* **6**, 6676 (2015).
- Andrews, S. FastQC: a quality control tool for high throughput sequence data. <http://www.bioinformatics.babraham.ac.uk/projects/fastqc> (2010).
- Dobin, A. et al. STAR: ultrafast universal RNA-seq aligner. *Bioinformatics* **29**, 15–21 (2013).
- Liao, Y., Smyth, G. K. & Shi, W. featureCounts: an efficient general purpose program for assigning sequence reads to genomic features. *Bioinformatics* **30**, 923–930 (2014).
- Ritchie, M. E. et al. limma powers differential expression analyses for RNA-sequencing and microarray studies. *Nucleic Acids Res.* **43**, e47 (2015).
- R Development Core Team. *R: a Language and Environment for Statistical Computing*. (R Foundation for Statistical Computing, Vienna, Austria, 2008).
- SEQC/MAQC-III Consortium. A comprehensive assessment of RNA-seq accuracy, reproducibility and information content by the Sequencing Quality Control Consortium. *Nat. Biotechnol.* **32**, 903–914 (2014).
- Hanbo, C. VennDiagram: generate high-resolution Venn and Euler plots. *The Comprehensive R Archive Network* <https://CRAN.R-project.org/package=VennDiagram> (2016).
- Cox, J. & Mann, M. MaxQuant enables high peptide identification rates, individualized p.p.b.-range mass accuracies and proteome-wide protein quantification. *Nat. Biotechnol.* **26**, 1367–1372 (2008).
- Cox, J. et al. Accurate proteome-wide label-free quantification by delayed normalization and maximal peptide ratio extraction, termed MaxLFQ. *Mol. Cell. Proteomics* **13**, 2513–2526 (2014).
- Tyanova, S. et al. The Perseus computational platform for comprehensive analysis of (prote)omics data. *Nat. Methods* **13**, 731–740 (2016).
- Nikić, I. et al. A reversible form of axon damage in experimental autoimmune encephalomyelitis and multiple sclerosis. *Nat. Med.* **17**, 495–499 (2011).
- Romanelli, E. et al. Cellular, subcellular and functional in vivo labeling of the spinal cord using vital dyes. *Nat. Protoc.* **8**, 481–490 (2013).

## Reporting Summary

Nature Research wishes to improve the reproducibility of the work that we publish. This form provides structure for consistency and transparency in reporting. For further information on Nature Research policies, see [Authors & Referees](#) and the [Editorial Policy Checklist](#).

### Statistical parameters

When statistical analyses are reported, confirm that the following items are present in the relevant location (e.g. figure legend, table legend, main text, or Methods section).

n/a Confirmed

- The exact sample size ( $n$ ) for each experimental group/condition, given as a discrete number and unit of measurement
- An indication of whether measurements were taken from distinct samples or whether the same sample was measured repeatedly
- The statistical test(s) used AND whether they are one- or two-sided  
*Only common tests should be described solely by name; describe more complex techniques in the Methods section.*
- A description of all covariates tested
- A description of any assumptions or corrections, such as tests of normality and adjustment for multiple comparisons
- A full description of the statistics including central tendency (e.g. means) or other basic estimates (e.g. regression coefficient) AND variation (e.g. standard deviation) or associated estimates of uncertainty (e.g. confidence intervals)
- For null hypothesis testing, the test statistic (e.g.  $F$ ,  $t$ ,  $r$ ) with confidence intervals, effect sizes, degrees of freedom and  $P$  value noted  
*Give  $P$  values as exact values whenever suitable.*
- For Bayesian analysis, information on the choice of priors and Markov chain Monte Carlo settings
- For hierarchical and complex designs, identification of the appropriate level for tests and full reporting of outcomes
- Estimates of effect sizes (e.g. Cohen's  $d$ , Pearson's  $r$ ), indicating how they were calculated
- Clearly defined error bars  
*State explicitly what error bars represent (e.g. SD, SE, CI)*

*Our web collection on [statistics for biologists](#) may be useful.*

### Software and code

Policy information about [availability of computer code](#)

Data collection

FACSDiva on the Fortessa LSRII used for flow cytometry experiments, softwares of Olympus FV1200 MPE microscope for in vivo experiments, software of FV1000 confocal microscopy system (Olympus) for fixed tissue acquisitions.

Data analysis

Adobe Photoshop v13, Adobe Illustrator v13, FIJI (ImageJ), GraphPad v7.03 (Prism), Excel plus10 (Microsoft), FlowJo v10 (BD), CASAVA1.8.2 (Illumina); Data filtering and statistical analysis for mass spectrometry was performed with Perseus v1.5.5.571, GraphPad Prism v7, Microsoft Excel plus10, and R Studio v3.4.0.

For manuscripts utilizing custom algorithms or software that are central to the research but not yet described in published literature, software must be made available to editors/reviewers upon request. We strongly encourage code deposition in a community repository (e.g. GitHub). See the Nature Research [guidelines for submitting code & software](#) for further information.

## Data

Policy information about [availability of data](#)

All manuscripts must include a [data availability statement](#). This statement should provide the following information, where applicable:

- Accession codes, unique identifiers, or web links for publicly available datasets
- A list of figures that have associated raw data
- A description of any restrictions on data availability

The data that support the findings of this study are available from the corresponding author upon reasonable request  
Full RNA sequencing dataset has been deposited online (GEO submission number is included in the text, GSE107792).

## Field-specific reporting

Please select the best fit for your research. If you are not sure, read the appropriate sections before making your selection.

Life sciences     Behavioural & social sciences     Ecological, evolutionary & environmental sciences

For a reference copy of the document with all sections, see [nature.com/authors/policies/ReportingSummary-flat.pdf](https://www.nature.com/authors/policies/ReportingSummary-flat.pdf)

## Life sciences study design

All studies must disclose on these points even when the disclosure is negative.

|                 |                                                                                                                                                                                                                                                                                                                                                           |
|-----------------|-----------------------------------------------------------------------------------------------------------------------------------------------------------------------------------------------------------------------------------------------------------------------------------------------------------------------------------------------------------|
| Sample size     | Although no power calculation was performed prior to study design, the number of mice used ensured statistically relevant results, as each animal used in this study provided thousands of events (i.e. single cells) to be analyzed. All number of mice and cell analyzed are reported in the respective sections (i.e. Figure Legends, Online methods). |
| Data exclusions | No data were excluded.                                                                                                                                                                                                                                                                                                                                    |
| Replication     | All the in vivo and in vitro experiments and most of the data analysis here reported have been executed separately and independently by 2 different researchers (GL and DT) to prove reproducibility of data.<br>All attempts of replicating results were successful.                                                                                     |
| Randomization   | Randomization was not possible due to the experimental design (i.e. Tomato and YFP reporters were guiding the cell selection in all experiments). However, all analysis were performed using images displayed on a gray scale, to avoid color-driven analysis bias.                                                                                       |
| Blinding        | Blinding was not possible due to the experimental design (i.e. Tomato and YFP reporters were guiding the cell selection in all experiments). However, all analysis were performed using images displayed on a gray scale, to avoid color-driven analysis bias.                                                                                            |

## Reporting for specific materials, systems and methods

### Materials & experimental systems

| n/a                                 | Involvement in the study                                        |
|-------------------------------------|-----------------------------------------------------------------|
| <input checked="" type="checkbox"/> | <input type="checkbox"/> Unique biological materials            |
| <input type="checkbox"/>            | <input checked="" type="checkbox"/> Antibodies                  |
| <input checked="" type="checkbox"/> | <input type="checkbox"/> Eukaryotic cell lines                  |
| <input checked="" type="checkbox"/> | <input type="checkbox"/> Palaeontology                          |
| <input type="checkbox"/>            | <input checked="" type="checkbox"/> Animals and other organisms |
| <input checked="" type="checkbox"/> | <input type="checkbox"/> Human research participants            |

### Methods

| n/a                                 | Involvement in the study                           |
|-------------------------------------|----------------------------------------------------|
| <input checked="" type="checkbox"/> | <input type="checkbox"/> ChIP-seq                  |
| <input type="checkbox"/>            | <input checked="" type="checkbox"/> Flow cytometry |
| <input checked="" type="checkbox"/> | <input type="checkbox"/> MRI-based neuroimaging    |

## Antibodies

### Antibodies used

Stainings were performed in ice-cold PBS after Fc-receptor blockade (CD16/32, 1ul/million cells, clone 2.4G2, BD Biosciences, Catalog No.553142) using LIVE/DEAD staining (Invitrogen, catalog number L34961) and the following antibodies: CD45 (clone 30-F11, BioLegend, 1:650, catalog number 103124), CD11b (clone M1/70, BD Biosciences, 1:500, Catalog No.557657), CD11c (clone N418, Abcam, 1:200, Product code ab111469), F4/80 (clone BM8, eBiosciences, 1:200, catalogue number 123116), Ly6C (clone AL21, BD Biosciences, 1:200, Catalog No. 560595), Ly6G (clone 1A8, Biolegend, 1:300, cat n. 127618), CD40 (clone HM40-3,

Biolegend, 1:200, cat n. 102912), MHC-II (clone M5/114.15.2, BD Bioscience, 1:250, Catalog No. 563414), CD80 (clone 16-10A1, Biolegend, 1:200, cat n. 104714) and CD86 (clone GL-1, Biolegend, 1:250, cat n. 105026). Samples were acquired on a LSR-Fortessa cytometer (BD Biosciences) and results analyzed by FlowJo software. For intracellular stainings, cells were incubated in complete RPMI supplemented with GolgiPlug (BD Biosciences) for 4 hours at 37°C and permeabilized with a Cytofix/Cytoperm kit (BD Biosciences) before staining with LAP (TGFb, clone TW7-16B4, Biolegend, 1:100, cat. n. 141405), TNFa (clone MP6-XT22, Biolegend, 1:100, Catalog No.563943), IL1Ra (clone EPR6483, Abcam, 1:100, Product code ab124962), and Il1b (NJTEN3, 1:100, Life Technologies LS25711482) specific antibodies.

#### Validation

All antibodies used are commercially available, and all relevant informations are contained in the Online methods. CD45 (clone 30-F11, quality tested by BioLegend), CD11b (clone M1/70, BD Biosciences, QC Testing: Mouse Tested in Development: Human), F4/80 (clone BM8, eBiosciences, quality control tested by immunofluorescent staining with flow cytometric analysis), Ly6C (clone AL21, BD Biosciences, reference: Cerwenka A, Carter LL, Reome JB, Swain SL, Dutton RW. In vivo persistence of CD8 polarized T cell subsets producing type 1 or type 2 cytokines. *J Immunol.* 1998; 161(1):97-105), Ly6G (clone 1A8, Biolegend, quality control tested by immunofluorescent staining with flow cytometric analysis), CD40 (clone HM40-3, Biolegend, quality control tested by immunofluorescent staining with flow cytometric analysis), MHC-II (clone M5/114.15.2, QC tested by BD Bioscience), CD80 (clone 16-10A1, Biolegend, quality control tested by immunofluorescent staining with flow cytometric analysis.) and CD86 (clone GL-1, Biolegend, quality control tested by immunofluorescent staining with flow cytometric analysis). Samples were acquired on a LSR-Fortessa cytometer (BD Biosciences) and results analyzed by FlowJo software. For intracellular stainings, cells were incubated in complete RPMI supplemented with GolgiPlug (BD Biosciences) for 4 hours at 37°C and permeabilized with a Cytofix/Cytoperm kit (BD Biosciences) before staining with LAP (TGFb, clone TW7-16B4, Biolegend, Oida T, et al. 2010. *PLoS One* 5:e15523), TNFa (clone MP6-XT22, Biolegend, Abrams J. Immunoenzymetric assay of mouse and human cytokines using NIP-labeled anti-cytokine antibodies. *Curr Protoc Immunol.* 2001; 1:6.20-6.21), and Il1b (NJTEN3, Life Technologies, tested by flow cytometric analyses of stimulated mouse thioglycolate-elicited peritoneal exudate cells) specific antibodies.

Antibodies were properly titrated to the right concentration prior to experimental used. The stainings were either validated by isotype controls or by use of genetically negative animal controls (i.e. for Tomato and YFP expressions) or by internal populations negative for specific stainings (i.e. for CD11b and CD45 stainings).

## Animals and other organisms

Policy information about [studies involving animals](#); [ARRIVE guidelines](#) recommended for reporting animal research

#### Laboratory animals

C57BL/6 mice were obtained from Janvier Labs (Saint Berthevin Cedex, France). In addition we used the following genetically modified mouse lines: iNOS-tdTomato-cre mice, Arginase-YFP mice (C.129S4/(B6)-Arg1tm1Lky/j), CD68-GFP mice (C57BL/6-Tg(CD68-EGFP)1Drg/j), Rosa26-Stp-fl-YFP mice (B6.Cg-Gt(Rosa)26Sor<tm3(CAG-EYFP)Hze>/J), CCR2RFP/+ mice (B6.129(Cg)-Ccr2tm2.1lfc/J) and CX3CR1GFP/+ mice (B6.129P-Cx3cr1tm1Litt/J). All genetically modified mouse lines except for the iNOS-tdTomato-cre were obtained from The Jackson laboratory (Bar Harbor, Maine). In all experiments, adult animals (minimum 6 weeks of age, maximum 5 months of age, mean 10 weeks of age) from both sexes were used. All in vivo manipulations were performed following either KX or MMF-induced anaesthesia. All animal experiments were performed in accordance with regulations of the relevant animal welfare acts and protocols approved by the respective regulatory bodies.

#### Wild animals

No wild animals were used.

#### Field-collected samples

No field-collected samples were used in this study.

## Flow Cytometry

### Plots

Confirm that:

- The axis labels state the marker and fluorochrome used (e.g. CD4-FITC).
- The axis scales are clearly visible. Include numbers along axes only for bottom left plot of group (a 'group' is an analysis of identical markers).
- All plots are contour plots with outliers or pseudocolor plots.
- A numerical value for number of cells or percentage (with statistics) is provided.

### Methodology

#### Sample preparation

For analysis of cell populations in the CNS, mice were sacrificed, CNS isolated and transferred to ice-cold PBS (Sigma-Aldrich). Tissue was cut in small pieces and digested in RPMI containing 2% fetal calf serum (Sigma-Aldrich), 25mM HEPES (Sigma-Aldrich), DNase I (10ng/ml, StemCell Technologies) and Collagenase D (0.8mg/ml, Roche) for 30' at 37°C. Reaction was stopped by adding 1:100 dilution of a 0.5M EDTA (Sigma-Aldrich) solution. Suspension was filtered through 70µm cell strainers (Falcon) and resuspended in a 30% solution of Percoll (Sigma-Aldrich). After 30' of gradient centrifugation at 12.000 g, the top (myelin) and lower (red cells) layers were removed and the remaining solution was filtered through 70µm cell strainers (Falcon). For blood analysis, blood was collected from the heart or submandibular vein in heparin-coated tubes. Erythrocytes were removed by incubation with FACS Lysing solution (BD Biosciences) for 10' on ice. For analysis of cell populations in lymph nodes, mice were sacrificed and the inguinal and axillary lymph nodes isolated and mechanically dissociated in ice-cold PBS (Sigma-Aldrich) using glass slides. The suspension was filtered through 70µm cell strainers (Falcon).

#### Instrument

Samples were acquired on a LSR-Fortessa cytometer (BD Biosciences)

|                           |                                                                                                                                                                                                                                                                                                                                                                                                                                                                                                                        |
|---------------------------|------------------------------------------------------------------------------------------------------------------------------------------------------------------------------------------------------------------------------------------------------------------------------------------------------------------------------------------------------------------------------------------------------------------------------------------------------------------------------------------------------------------------|
| Software                  | Results displayed/analyzed by FlowJo software. Data were later organized in GraphPad.                                                                                                                                                                                                                                                                                                                                                                                                                                  |
| Cell population abundance | Within the CD45hi-CD11bhi population isolated from iNOS-tdTomato-cre x Arginase-YFP mice at peak disease, $19 \pm 2.9$ for MiNOS, $18.6 \pm 1.6$ for MiNOS/Arginase and $8.7 \pm 1.3$ for MArginase cells.                                                                                                                                                                                                                                                                                                             |
| Gating strategy           | FSC/SSC gates were used to define a generic live lymphocytic/myeloid population. duplets were excluded. Dead cells were excluded (LIVE DEAD staining from invitrogen). Activated myeloid cells were defined as Cd11b high, CD45 high. Ly6g positive cells were excluded. For the sorting experiment, a further gating on CD115+ or CD64+ populations was applied. Distinct polarized cell gates were defined as YFP, Tomato, YFP/Tomato positive cells compared to B6 control mice with a comparable clinical disease. |

Tick this box to confirm that a figure exemplifying the gating strategy is provided in the Supplementary Information.